

## INFORMATION TO USERS

The most advanced technology has been used to photograph and reproduce this manuscript from the microfilm master. UMI films the original text directly from the copy submitted. Thus, some dissertation copies are in typewriter face, while others may be from a computer printer.

In the unlikely event that the author did not send UMI a complete manuscript and there are missing pages, these will be noted. Also, if unauthorized copyrighted material had to be removed, a note will indicate the deletion.

Oversize materials (e.g., maps, drawings, charts) are reproduced by sectioning the original, beginning at the upper left-hand corner and continuing from left to right in equal sections with small overlaps. Each oversize page is available as one exposure on a standard 35 mm slide or as a 17" x 23" black and white photographic print for an additional charge.

Photographs included in the original manuscript have been reproduced xerographically in this copy. 35 mm slides or 6" x 9" black and white photographic prints are available for any photographs or illustrations appearing in this copy for an additional charge. Contact UMI directly to order.



Accessing the World's Information since 1938

300 North Zeeb Road, Ann Arbor, MI 48106-1346 USA



Order Number 8805575

**Direct simulation of hypersonic transitional flows over blunt  
slender bodies**

Cuda, Vincent, Jr., Ph.D.

Old Dominion University, 1987

**U·M·I**  
300 N. Zeeb Rd.  
Ann Arbor, MI 48106



**PLEASE NOTE:**

In all cases this material has been filmed in the best possible way from the available copy.  
Problems encountered with this document have been identified here with a check mark ☒.

1. Glossy photographs or pages \_\_\_\_\_
2. Colored illustrations, paper or print \_\_\_\_\_
3. Photographs with dark background \_\_\_\_\_
4. Illustrations are poor copy \_\_\_\_\_
5. Pages with black marks, not original copy ☒
6. Print shows through as there is text on both sides of page \_\_\_\_\_
7. Indistinct, broken or small print on several pages \_\_\_\_\_
8. Print exceeds margin requirements \_\_\_\_\_
9. Tightly bound copy with print lost in spine \_\_\_\_\_
10. Computer printout pages with indistinct print \_\_\_\_\_
11. Page(s) \_\_\_\_\_ lacking when material received, and not available from school or author.
12. Page(s) \_\_\_\_\_ seem to be missing in numbering only as text follows.
13. Two pages numbered \_\_\_\_\_. Text follows.
14. Curling and wrinkled pages \_\_\_\_\_
15. Dissertation contains pages with print at a slant, filmed as received \_\_\_\_\_
16. Other \_\_\_\_\_  
\_\_\_\_\_  
\_\_\_\_\_

University  
Microfilms  
International



DIRECT SIMULATION OF HYPERSONIC TRANSITIONAL FLOWS  
OVER BLUNT SLENDER BODIES

by

Vincent Cuda, Jr.  
B.S. May 1980, Old Dominion University  
M.E. December 1982, Old Dominion University

A Dissertation Submitted to the Faculty of  
Old Dominion University in Partial Fulfillment of the  
Requirements for the Degree of

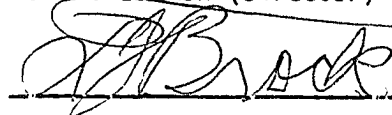
DOCTOR OF PHILOSOPHY

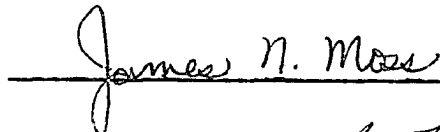
MECHANICAL ENGINEERING

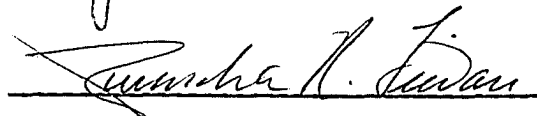
OLD DOMINION UNIVERSITY  
August 1987

Approved by:

  
Robert L. Ash (Director)









ABSTRACT

DIRECT SIMULATION OF HYPERSONIC TRANSITIONAL FLOWS  
OVER BLUNT SLENDER BODIES

Vincent Cuda, Jr.  
Old Dominion University, 1987  
Director: Dr. Robert L. Ash

Hypersonic transitional flow has been studied using the Direct Simulation Monte Carlo method. The cylindrically blunted wedge and spherically blunted cone were examined for body half angles of  $0^\circ$ ,  $5^\circ$  and  $10^\circ$ , at a flight velocity of 7.5 km/s, zero angle of incidence and altitudes of 70 to 100 km. Those geometries and flow conditions are important considerations for hypersonic vehicles currently under design. Surface chemistry was examined for diffuse, finite-catalytic surfaces. Nonequilibrium chemistry and nonequilibrium thermodynamics were considered for both configurations at all altitudes.

Numerical simulations showed that rarefied gas effects, such as surface temperature jump and velocity slip, exist. Slip conditions were more significant for the axisymmetric cases and the onset of chemical dissociation occurred first for the two-dimensional configuration at 96 km. Comparisons between the numerical simulation and viscous shock-layer calculations at the higher altitudes show significant differences in the calculated heat-transfer rate, body drag and flowfield structure. A comparison with hypersonic wind tunnel heat-transfer rate data showed good agreement.



DEDICATION

To Nancy.

#### ACKNOWLEDGEMENTS

I wish to express my appreciation to Dr. R. L. Ash for his part in the direction and supervision of this work and for the encouragement provided me during the course of my Doctoral program.

I thank F. J. Brock for his numerous discussions in the fields of physics, mathematics and computer systems. His assistance in editing and outlining the dissertation are greatly appreciated.

I also wish to express my appreciation to Dr. J. N. Moss who supervised the numerical simulations and data evaluation, to J. E. Hueser for his assistance in providing the contour plotting routines used in this text, and to Dr. G. A. Bird for his many helpful discussions.

## TABLE OF CONTENTS

	Page
LIST OF TABLES.....	vi
LIST OF FIGURES.....	vii
LIST OF SYMBOLS.....	ix
 Chapter	
1. INTRODUCTION.....	1
1.1 Hypersonic Research and Transitional Flows.....	1
1.2 Nonequilibrium Hypersonic Flows.....	3
1.3 Particle Approach for Gas Dynamics Problems.....	5
1.4 Molecular Interaction Potentials.....	7
1.5 Molecular Internal Degrees of Freedom.....	9
1.6 Evolution of the Particle Approach Concept.....	11
1.7 Motivation for Current Research Effort.....	14
2. DISCUSSION OF THE DIRECT SIMULATION MONTE CARLO METHOD..	16
2.1 Introduction to the DSMC Method.....	16
2.2 Cell Criteria.....	19
2.3 Equations and Processes.....	23
2.4 Numerical Inputs.....	30
2.5 Computational Considerations in the Use of DSMC....	31
3. PROBLEM FORMULATION.....	33
3.1 Computational Code.....	33

## TABLE OF CONTENTS (CONCLUDED)

<u>Chapter</u>	<u>Page</u>
3.2 Numerical Inputs for Current Study.....	37
3.3 Geometry and Flow Conditions.....	42
3.4 Viscous Shock Layer Calculations.....	43
4. RESULTS AND DISCUSSION.....	47
4.1 Knudsen Number.....	47
4.2 Two-Dimensional Flows.....	49
4.3 Comparison of Two-Dimensional and Axisymmetric Results.....	62
4.4 Comparison of DSMC and Viscous Shock Layer Calculations.....	74
4.5 Comparisons Between Calculations and Experiments.....	84
5. CONCLUSIONS.....	88
REFERENCES.....	91
APPENDICES	
A. MASS FLUX CONSERVATION .....	98
B. KNUDSEN NUMBER.....	101

## LIST OF TABLES

TABLE	PAGE
3.1. Reaction rate coefficients.....	39
3.2. Representative gas properties.....	44
3.3. Freestream conditions.....	45
3.4. Freestream parameters and surface coefficients.....	45

## LIST OF FIGURES

FIGURE	PAGE
2.1 Computational domain for 2-D and axisymmetric configurations.....	20
2.2 Test particle in a stationary gas.....	25
3.1 Flow chart of the computational code.....	34
4.1 Local Knudsen number along the 2-D stagnation streamline.....	48
4.2 Effect of rarefaction upon the 2-D stagnation streamline density profiles.....	50
4.3 Effect of rarefaction upon the 2-D stagnation streamline normal velocity profiles.....	51
4.4 Extent of thermodynamic nonequilibrium along the 2-D, 70 km stagnation streamline.....	53
4.5 Species mass fractions along the 2-D, 70 km stagnation streamline.....	54
4.6 Overall kinetic temperature contours for the blunt flat plate at 85 km .....	56
4.7 Number density contours for the blunt flat plate at 85 km ( $n = 1.65 \times 10^{20} \text{ m}^{-3}$ ).....	57
4.8 Temperatures adjacent to the blunt flat plate at 85 km, $s/R_N = 0$ .....	58
4.9 Temperatures adjacent to the blunt flat plate at 85 km, $s/R_N = 4.1$ .....	59
4.10 Effect of rarefaction on the 2-D wall pressure coefficient.....	60
4.11 Effect of rarefaction on the 2-D heat-transfer coefficient.....	61
4.12 Effect of wedge angle on pressure distributions for the 2-D flat plate at 85 km.....	63

# LIST OF FIGURES (CONCLUDED)

FIGURE	PAGE
4.13 Effect of wedge angle on the heat-transfer rate distributions for the 2-D flat plate at 85 km.....	64
4.14 Effect of rarefaction on the temperature jump at the stagnation point for the 2-D flat plate at 85 km.....	65
4.15 Effect of rarefaction on the temperature jump at $s/R_N = 4.1$ for the 2-D flat plate at 85 km.....	66
4.16 Effect of rarefaction on the velocity slip at $s/R_N = 4.1$ .....	68
4.17 Stagnation line Knudsen number variation for the wedge and cone at 70 km.....	69
4.18 Maximum atomic mass fraction values along the stagnation streamline.....	70
4.19 Stagnation point heat-transfer coefficient versus freestream Knudsen number.....	72
4.20 Drag coefficient versus freestream Knudsen number.....	73
4.21 Comparison of the calculated stagnation streamline density for the VSL and DSMC 5° cones at 70 km.....	75
4.22 Comparison of the stagnation streamline temperature for the VSL and DSMC 5° cone at 70 km.....	76
4.23 Stagnation streamline species mass fraction distributions for the DSMC 5° cone at 70 km.....	77
4.24 Comparison of the stagnation streamline atomic mass fraction distributions for the VSL and DSMC 5° cones at 70 km.....	79
4.25 Comparison of the calculated density profiles for the VSL and DSMC 5° cone at 80 km.....	80
4.26 Comparison of the overall temperature for the VSL and DSMC 5° cone at 80 km.....	82
4.27 Comparison of the tangential velocity for the VSL and DSMC 5° cone at 80 km ( $s/R_N = 4.1$ ).....	83
4.28 Comparison of experimental and DSMC method heat-transfer rate for the spherically blunted cylinder.....	85

# LIST OF SYMBOLS

a	constant in the reaction rate equation
$A_b$	base
b	constant in the reaction rate equation
$C_D$	drag coefficient, $2F/\rho_\infty U_\infty^2 A_b$
$C_H$	heat-transfer coefficient, $2q/\rho_\infty U_\infty^3$
$C_i$	mass fraction of species i, $\rho_i/\rho$
$C_p$	pressure coefficient, $2p/\rho_\infty U_\infty^2$
$C_r$	relative velocity
$C^*$	$\mu^* T_\infty / \mu_\infty T^*$
e	energy
$E_a$	activation energy
F	force
$F_{num}$	scaling factor equivalent to the number of physical molecules to computational molecules
K	reaction rate
k	Boltzmann constant
Kn	Knudsen number, $\lambda/l$ or $(\lambda/\rho)(dp/dn)$
$K_r^2$	Cheng's parameter, $p_\infty R_M / \mu_\infty U_\infty C^*$
$l$	characteristic dimension
M	Mach number, $U/\sqrt{\gamma RT}$
$\bar{M}$	molecular weight of mixture
m	mass



$N$	number of molecules
$N_c$	number of collisions
$N_m$	number of model molecules
$n$	number density
$p$	pressure
$q$	heat flux
$R$	universal gas constant, $R = 8.3143 \text{ J/mol K}$
$R_B$	base radius
$R_N$	nose radius
$Re_\infty$	Reynolds number, $\rho_\infty U_\infty R_N / \mu_\infty$
$s$	coordinate along body surface
$S_\infty$	speed ratio, $U_\infty / \sqrt{2RT_\infty}$
$T$	thermodynamic temperature
$T_{ov}$	overall kinetic temperature
$T_{rt}$	rotational kinetic temperature
$T^*$	$(T_{O,\infty} + T_w)/2$
$t$	time
$u$	velocity component tangent to body surface
$U_\infty$	freestream velocity
$V$	volume
$v$	velocity component normal to surface
$w$	velocity component in the $z$ direction
$X_i$	mole fraction of species $i$
$x$	coordinate measured along the body centerline
$y$	coordinate measured normal to the body centerline
$z$	coordinate measured along the body width
$\Gamma$	gamma function

$\gamma$	ratio of specific heats
$\varepsilon$	$\sqrt{\mu_{ref}/\rho_{\infty}U_{\infty}R_N}$
$n$	coordinate normal to body surface
$\theta$	body half angle
$\lambda$	mean free path
$\mu$	viscosity
$\mu^*$	viscosity evaluated at $T^*$
$\nu$	collision frequency
$\rho$	density
$\sigma_T$	collision cross section
$\sum$	summation
$\omega$	the temperature exponent in the viscosity power law relation

#### Subscripts

c	collision
ref	reference
i	ith species
w	wall values
$\infty$	freestream values
o	total values

#### Abbreviations

DSMC	Direct Simulation Monte Carlo
AOTV	aeroassisted orbital transfer vehicles
MFP	mean free path
TAV	transatmospheric vehicle
VSL	viscous shock layer
2-D	two-dimensional

## Chapter 1

### INTRODUCTION

#### 1.1 Hypersonic Research and Transitional Flows

Numerical research in hypersonic fluid dynamics was directed originally toward reentry vehicle design. From the 1950's to the early 1960's, intercontinental ballistic missiles and the Apollo spacecapsule were of primary concern [1].\* Both were blunt bodies that dissipated heat during the descent stage of their trajectories at high altitudes where atmospheric density is very low (rarefied). Those flows were modeled using free molecular relations. The study of rarefied gas dynamics, using a variety of methods was developed at that time because spacecraft design could be studied using some rather elegant mathematics without using large computers. Methods included the extension of free molecular flow theory to include the effects of molecular collisions in the gas [2]. Similarity solutions [3] and a reduced set of Navier-Stokes equations [4] were developed and applied to low density flows and mathematical solutions to the Boltzmann equation were also formulated [5,6].

More recently, space shuttle [7] has expanded both the required geometrical configurations and flowfield envelope in hypersonic

---

\*The numbers in brackets indicate references.

research. A significant portion of the shuttle flight trajectory is subject to atmospheric densities at intermediate altitudes where the flow departs from continuum but does not allow free molecular flow approximations. These flows are not modeled properly using simple free molecular relations because significant levels of molecular interaction (collisions) are still present. This flow regime is called transitional flow [8-11] and must consider particle collisions (dense gas effects) and surface interactions at the molecular level (rarefied gas effects). Collision and surface scattering are important phenomena in transitional flows but they represent competing extremes from the standpoint of theoretical models. Few methods are available for the study of transitional flows, and the incorporation of velocity slip and temperature jump, in continuum analysis, is considered sufficient for most design applications to date [11-14]. However, current problems stretch the limits of those assumptions.

In order to illustrate further the behavior of a transitional flow, a brief examination of physical flow length scales is helpful. The mean free path of a flow is the average distance travelled by molecules between collisions. The collision frequency is defined as the number of collisions per unit time. For an equilibrium gas, this becomes the mean thermal speed divided by the mean free path. For ambient conditions on Earth, the mean free path is on the order of hundreds of angstroms and the flowfield is considered to be in a state of thermal equilibrium because the collision frequency adjusts information flow over small spatial dimensions. However, when low densities are encountered, such as the case for orbital or reentry flight, the average distance between successive molecular collisions may be larger than the physical

dimensions of objects in the flow. Thus, for flows where the density is increasing or decreasing, the collision frequency changes and there may be insufficient collisions to maintain equilibrium.

Current research required for the design of aeroassisted orbit transfer vehicles (AOTV) and high speed transatmospheric vehicles (TAV) has necessitated the development of computational models for the study of transitional flows at hypersonic speeds [15]. Basic aerodynamic models for high lift to drag ratio vehicles are of primary concern, and reliable data in the transitional flow regime are an important need. Many vehicle shapes are slender and elongated and their leading edges will be subjected to very high temperatures. Their surfaces can become catalytic in much of the operational range of interest as particles strike the body and release or absorb energy sufficient to cause chemical reactions to take place [16-18]. Because of the relatively low molecular populations present in the flowfield, surface chemistry cannot be ignored since it alters heating rates and pressure distributions measurably. In fact, it can control material selection in system designs [19,20].

### 1.2 Nonequilibrium Hypersonic Flows

The problem common to these new hypersonic applications is the nonequilibrium nature of the flow for some portions of the flight. Even though peak heating and primary maneuvering may occur under essentially continuum conditions for most reentry trajectories [21], some parts of the flowfield are rarefied, particularly the leading edges or the nose region of the vehicle. Under hypersonic conditions, the shock wave is a highly nonequilibrium region independent of the altitude [22-24], and for this type of high velocity flight, the local fluid temperature is

not unique [25-27]. An additional concern is the extent of validity of the equations of state in the description of the gas at hypersonic speeds. Equations of state assume no internal gas structure and do not describe the collision process. These assumptions do not affect the accuracy of the gas description as long as the gas is in thermal equilibrium (same translational, rotational and vibrational temperature). State equations, however, are less useful in thermal nonequilibrium flows.

The study is complicated further by inclusion of significant equilibrium and nonequilibrium chemical reactions contained in the molecular population that preclude classical rarefied gas assumptions. Not only do the number and types of chemical reactions increase, but they also affect the pseudo-continuum transport properties. Previous studies have shown that the assumed linear relationship between the transport properties and the macroscopic flow variables (species concentration, velocity and temperature) is no longer valid [28-30].

From the molecular point of view, the internal energy adjustment lags the translational energy adjustment, resulting in thermal nonequilibrium. Elevated translational temperatures give rise to additional chemical reactions and can result in other chemical nonequilibrium effects. The types of hypersonic flows that are being studied today do not yield reliable predictions using either free molecular or continuum models. Characteristics of both regimes are important because they cannot be separated for a particular flow situation. Virtually all hypersonic transitional flows include nonequilibrium effects.

### 1.3 Particle Approach for Gas Dynamics Problems

The study of high speed, transitional flows must include aspects of continuum and rarefied flows and precludes an analysis with the Navier-Stokes equations. Computationally, there appears to be no alternative to the particle approach when local scale lengths are of the same order as a mean free path [31,32]. A particle approach can provide a numerical simulation capability within the transitional flow regime without exceeding existing computer capability.

A physical particle is either an atom which constitutes the basic unit of a chemical element, a molecule (a group of atoms held together by chemical forces), or an atom (molecule) that is charged, such as an ion or an electron. For purposes of discussion throughout this text the terms particle and molecule will be used interchangeably to refer to a neutral, spherical, mass point which exists by itself and retains all its chemical properties.

The particle description includes both external force fields and internal structure. Molecular collision dynamics can be modeled on a microscopic scale by making the three assumptions used in dilute gas theory [33]: (1) the particles are so widely spaced that the combined volume of the particles is much less than the total volume that they occupy, (2) the intermolecular forces are only important during the brief instant of collision and are neglected at all other times, and (3) the average duration of a collision is negligible with respect to the average time between collisions. These conditions imply that particles are independent of one another and exert no influence upon one another except in the brief instant of collision.

The basic processes that make up a physical flow are the motion of particles, particle interaction with rigid boundaries, the collision of particles with other particles and the associated energy transfer and chemical processes which occur during the collisions. Physical particles may experience all these processes simultaneously because intermolecular force fields are infinite in extent (each molecule is affected by all other molecules in a flowfield).

In order to address properly a particle approach where sets of molecules are modeled, flowfield parameters need to be formulated at the molecular level. Unlike a continuum gas where behavior is inferred from the solution of an integro-differential equation system describing the bulk properties of the gas, a particle approach must include information describing molecular properties of the individual species. Of primary interest is the need to simulate collision dynamics for sets of particles that represent realistic collections of molecular interactions. A particle must act as a single unit with a description similar to an atom (or molecule) of finite size and mass. The exact character of molecular force-fields is neither fully understood nor precisely modeled; however, each particle must have a properly defined force-field associated with its center of mass which interacts with other particle force-fields. A somewhat arbitrary distance (on the order angstroms) from the particle's center of mass is taken to be the distance of initial interaction. This distance is larger than the outermost electron orbit of the molecules so that a "collision" is in effect the overlapping of force fields and not necessarily that of electron orbits. The particle approach incorporates the molecular description into the computational model through a computational



particle that retains the identity of a representative physical particle. The computational model follows individual trajectories and models the collisions of computational particles, but it need not follow individual physical particles. Energy transfer and chemistry associated with collisions can be included for multi-specie gases. Further discussion on the computational particle and the algorithms that make up the various particle descriptions are provided in the remaining sections of this chapter. The discussion starts with descriptions of various molecular building blocks and proceeds through details of the principle particle approaches.

#### 1.4 Molecular Interaction Potentials

Intermolecular potential functions have been developed to describe the forces between two colliding particles. A large fraction of the work performed on the development of interaction potentials treats spherically symmetric molecules only. The most basic potential function is a rigid impenetrable sphere [34]. For purposes of illumination, consider a gas composed of particles that are distributed uniformly and held stationary in a volume with respect to a test particle. (A test particle is defined here as a particle which enters the flowfield and is not to be confused with the Test Particle Method to be described later.) The "stationary" particles present themselves as targets and the ability of the test particle to hit targets in a given unit of time is related not only to the size of the targets but also to the relative speed of the test particle to the target particles.

A hard sphere collision is assumed to occur when particles are separated by a distance corresponding to the sum of the distances from the particles' centers. A collision cross-section can be calculated

using that separation distance, and it is assumed that the two particles can collapse no further. Hence, an infinite force is applied during the encounter and approximates the short-range, repulsive force while neglecting the long-range, attractive force. The assumptions incorporated in the rigid sphere model do not account for the dependency of the interaction energy upon the interaction force, the energy transfer to the internal energies of the molecule or the non-symmetrical geometry of the physical molecule.

Attempts to devise potential functions with adjustable parameters, representing a more realistic collision process have been summarized briefly by Macrossan [35]. However, to account for three-dimensional motion of non-spherical molecules over a range of particle interaction energies requires a prohibitive number of adjustable parameters. Molecular models suitable for describing a real gas are more useful if they retain only the essential molecular properties. Most often, molecules are considered as spheres that obey an isotropic scattering law and result in a uniform scattering angle distribution independent of the molecular velocities. Some models in current use [36-39] include energy dependent variables that describe the short range, repulsive and long-range, attractive forces which govern molecular interactions. All of these models depend on laboratory verification and are limited to a moderate range of particle energies.

The ultimate goal of any molecular model is to predict correctly the way an energy dependent collision cross-section affects the transport properties. Since any attempt to describe molecular collisions must include laboratory measurements, a basic approach involves a scheme that yields the measured viscosity of a gas over a range of particle

energies. This can be achieved by using a hard sphere model, the diameter of which depends on the collision energy. This approach does not require an explicit determination of the transport properties; they are determined after the evolution of the solution.

The Variable Hard Sphere (VHS) model can be used to compute real gas flow molecular cross-sections. The variation in cross-section with collision energy can be determined from the measured viscosity variation with temperature. The Chapman-Enskog Theory [31] can be used to relate the hard sphere cross-section to viscosity. In this approach, the cross-section is assumed to vary with temperature according to a power law (between -0.4 and -0.1 for most common gases). For reference, the rigid hard sphere model merely neglects temperature dependence while a Maxwell molecule model predicts a negative  $1/2$  temperature exponent. The value of the exponent for a real gas is determined from experimental measurements of the viscosity of the gas. However, in the variable hard sphere model, no distinction in the exponent is made for individual species. The exponent is assumed constant for all calculations and represents the single, best-estimate for all species in the gas. This model works well in predicting density profiles across shock waves [40]. The VHS molecular model uses the isotropic scattering assumption (uniform scattering angle distribution) since laboratory data indicates the mass flow properties are weakly sensitive to the model scattering angle distribution.

### 1.5 Molecular Internal Degrees of Freedom

In addition to the kinetic energy associated with motion, available internal degrees of freedom participate in the total energy transfer in the collision process. The inclusion of molecular rotation and

vibration become necessary when the flow includes molecules composed of more than a single atom. The most complete mathematical description of the motion of a particle is found in the quantum-mechanical description provided by the Schrödinger equation. A prohibitively large (essentially infinite) computation effort for even the simplest of atoms (like hydrogen) is required because each subatomic particle (electrons, protons, neutrons, etc.) requires an integro-differential equation solution to provide population assignments for the available energy states. In gas dynamics, a quantum-mechanical description of gas flows cannot be considered unless events that occur very rarely need to be described.

Statistical mechanics can be used to provide a macroscopic description of the energies in an equilibrium flow by summing over all possible energy states and assigning an average energy to the flow [41]. The result is the Boltzmann distribution which through a statistical mean provides the fraction of the total energy assigned to the internal energies. It does not attempt to keep track of individual particle energy states and provides no means of assigning external or internal energies to individual species.

Phenomenological models can be used as a mechanism for driving the energy-per degree of freedom to an equilibrium value. These models make no attempt to describe the structure of a particle, however, through molecular collisions, Maxwellian distributions for gases are achieved. The sorting of energy through the phenomenological model drives the energy modes toward a mean, equilibrium value because high energy states are biased towards low energy states and low energy states are biased towards high states through random collision exchanges.

### 1.6 Evolution of the Particle Approach Concept

The particle approach concept was first developed in the fields of optics [42,43] and nuclear physics [44] where ray tracing techniques (later called test particle methods [45]) were used in the analysis of short-wavelength propagation in random media. Photons were followed as they traveled in a prescribed media to provide estimates of measurable quantities from a representative sampling of rays. These techniques were applied to gas dynamics by Davis [45] where gas particle trajectories (instead of photon trajectories) were calculated. An initial estimate of the gas velocity distribution function provided the velocity assignments for simulated particles generated at flux boundaries. Those particles were sent through the flow domain on an individual basis and were allowed to reflect off boundary surfaces. Thermal accommodation created new velocity assignments by centering the thermal speeds of the reflected particles about the wall temperature. The two fluxes in the flow domain (the undisturbed distribution and the reflected distribution) served as the flow variables. The reflected particles were an additional contribution to local number densities. Particle insertion was allowed to continue until there was no significant adjustment in the reflected particle distribution. The number density at any point in space was obtained by evaluating the normal component of the number fluxes through a surface containing that point and evaluating the net flux across that surface.

The formulation of the Test Particle Method made no provision for the assessment of intermolecular collisions. Particles were inserted serially over a small time interval so that the insertion rate could approximate the actual physical flux. The magnitude of the computation

requirement was directly proportional to the number of trajectories compiled, and an iteration for the initial starting flow was required. Because of the difficulty in estimating the initial flowfield conditions and in taking into account the assumptions made in the numerical formulation, the Test Particle Method has been used primarily in collisionless, one-dimensional steady flow problems [45].

The Molecular-Dynamics Method developed by Alder and Wainwright [46] is a direct extension of the ray tracing technique. Individual gas particles were followed as they traversed a computational domain and their behavior included the effects of molecule-molecule collisions. This was achieved through replacing a large number of physical particles in a region of physical space with a smaller number of simulated particles in a computational space. The initial placement of particles was set randomly, but all subsequent calculations were performed deterministically. Collisions occurred when force-fields overlapped and the post-collision trajectories were determined from particle location and pre-collision velocity data. The computation requirements were proportional to the square of the number of simulated particles, since each trajectory was influenced by all other particles. (They were all potential collision partners.) In order to properly account for flow processes, an appropriate number of particles was required in the simulated flowfield.

A computational particle models a small number of physical particles by representing the total volume of the physical particles (the model creates a small number of "large" particles). The estimation of the required number of computational particles is based on the smallest computational domain in the Molecular-Dynamics Method [46]

which is the cubic mean free path. The number of particles in a cubic mean free path is inversely proportional to the square of the density [47]. In a dense gas (like sea level atmospheric conditions), the local mean free path is small and the cubic mean free path is occupied by several thousand physical particles. As density decreases, the number of physical particles per cubic mean free path increases. For example, at a 100 km altitude,  $3 \times 10^{16}$  particles are present in each cubic mean free path. Since the computation of a large number of particles is prohibitive, a smaller set of large particles is used. Bird [47] has shown that the volume of the computational particle (for a dilute gas), as normalized by the cubic mean free path, should be much smaller than unity. As density decreases, the size of the model particle approaches the dimensions of the local mean free path, and the dynamics of the simulated collision processes no longer models the physics. It is for this reason that the Molecular-Dynamics method is confined to dense gas analyses [32, 47]. The coupling of the motion and collision processes results in computational times that are directly proportional to the square of the number of simulated particles. Evaluation of all potential collision partners is required to find the most probable collision pair. By considering motion and collisions simultaneously the simulated collision frequency approaches (in the limit of a large number of simulated particles) the physical collision frequency of the gas.

The Direct Simulation Monte Carlo method [31,32] evolved from the Molecular-Dynamics concept by considering the motion and collision processes through a two-step procedure (uncoupled processes). The motion process moves the molecules according to their velocities and the collision process models collisions through probabilistic means.

Computation time is then directly proportional to the number of simulated particles because of the uncoupling of the collision model. By evaluating (sampling randomly) only two molecules at a time as a potential collision pair, the computational speed is increased because fewer evaluations are required in choosing potential collision pairs.

The two-step process is valid if small differences between the simulated and physical collision frequency are maintained. Physical collision frequency is preserved by examining both processes over computational time steps which are much smaller than the actual time between typical collisions. Since collisions do not occur (on the average) over these small increments of time, the influence of the computational model on the true collision frequency is minimal. The uncoupling of the simulated processes results in a simulated collision of particles which must preserve the statistical mean of the physical collision frequency. With a physically correct collision frequency and a deterministic evaluation of molecular trajectories, the simulated gas flow can be a faithful description of the physical processes.

### 1.7 Motivation for Current Research Effort

The flowfield structure and aerothermodynamic characteristics of blunt cones and wedges is well represented in the literature. A few hypersonic transitional flow studies are available for axisymmetric geometries [48-50]. These studies yield insight into the behavior of the flowfield; however, no systematic investigation to date has considered the study of a blunt slender body through a range of flight conditions that cover the full transitional flow regime. Both axisymmetric and two-dimensional configurations are considered for highly energetic flows which are beyond investigation using current wind



tunnel facilities. The flowfields of these geometries are compared to each other for identical flight conditions and represent a research effort unavailable in the literature.

In addition, the current work provides the chemical and thermodynamics nonequilibrium description of a high-speed flow over a two-dimensional blunt body. No literature is currently available for this study through the particle approach method.

A third motivation is to delineate flow regions which can be described adequately by continuums. Early attempts to indicate noncontinuum flows through the use of a Knudsen number\* fail to address the local flowfield behavior of vehicles in flight. Gas flow departure from the continuum description is indicated using the local Knudsen number and through the onset of the velocity slip and temperature jump.

The Direct Simulation Monte Carlo Method has been used in this study and the formulation of the model is developed in the next chapter. Details of that formulation, as applied to a numerical simulation, are addressed in Chap. 3.

---

\*The definition of Knudsen number is given by dividing the mean free path,  $\lambda$ , by some characteristic length,  $l$ , such as a body dimension which physically determines the flow.

## Chapter 2

### DISCUSSION OF THE DIRECT SIMULATION MONTE CARLO METHOD

#### 2.1 Introduction to the DSMC Method

The Direct Simulation Monte Carlo (DSMC) method was developed by Graeme A. Bird [31]. It is direct in that the method models the physics directly (not through an integro-differential equation system) and it is a Monte Carlo method in that it uses a probabilistic approach. It does not solve the Boltzmann equation but has been demonstrated to yield a solution which is equivalent to the solution of the time-dependent Boltzmann equation [51].

Real gas flows are modeled computationally by simulating large numbers of model particles. Each model particle represents a set of physical particles. Model particles (also known as computation particles or simulated molecules) take on the character of physical particles by retaining the mass, volume and internal structure of the molecules. Particles are assigned position coordinates, velocities and an internal structure which is assumed identical for all members of the particle. Each model particle represents only one specie. Though the physical particle may be complex in geometry, the model particle is assumed to be spherical. Hence, a model particle represents a large set of identical physical particles, each with identical characteristics (cross-sections, energy states, etc.). For example, for ambient

conditions at an altitude of 100 km proper resolution may require as many as  $10^4$  computational particles to represent the  $10^{19}$  physical particles in a physical flow. (In this case, one model particle represents  $10^{15}$  physical particles). The  $10^4$  model particles are necessary to retain proper representations of the various species and their energy distributions. A computational domain is required in physical space to facilitate the choice of potential collision pairs and the sampling of the macroscopic flow properties. Advantage is taken of flow symmetries to reduce the number of position coordinates that are stored for each particle. The simulation does not require an initial approximation to the flowfield. It is normally started with the computational volume completely empty (vacuum) or the volume is part of an infinite domain and is populated by sampling from a prescribed distribution function. Particles enter the computational domain through prescribed boundary fluxes. Particle motion is monitored and position coordinates are updated for each computational time step. Particles are permitted to collide with surfaces and reflect in either a diffuse or specular manner (or a prescribed mixture of diffuse and specular reflections). Computer storage space for particles that leave the computational domain is reassigned to particles that enter the flowfield during subsequent time steps. Complex boundaries are easily modeled and the computational domain can be applied to two- or three-dimensional configurations.

The collision processes associated with a real gas are incorporated at the molecular level. Individual particles are selected randomly from the domain as candidates for a collision, without referring to the other particles in the flowfield. Collisions are probabilistic events weighted according to the potential collision pair's relative speed. A

large relative speed is more likely to result in a collision because the distance traversed by the pair is greater per unit of time than a pair with a small relative speed. Collision pairs are also weighted to reproduce the concentration of the participating species in each cell. Since the collision processes are uncoupled from the motion process, the original and final locations in computational space remain unchanged; only the velocities are updated.

Internal structure is approximated indirectly through prescribed relaxation rates which are assigned to the gas. Here relaxation is defined as a process by which the gas approaches an equilibrium state after conditions affecting it have changed suddenly. The numerical simulation can model reacting gases and accuracy is based on the ability to describe properly the individual species at the molecular level. Chemical identity is retained through assignment of internal degrees of freedom, steric factors, heats of reaction and characteristic temperatures. This description corresponds to classical approaches where a reaction rate equation is incorporated in the kinetic equations.

All events are treated as unsteady events. Sampling of flowfield parameters such as number density and velocity is performed when the solution reaches a simulated steady state which is defined as a flow state that does not change statistically with time. To date, no stability problems common to the solution of a system of differential equations have been observed.

The DSMC method has evolved over the past 25 years through application of the technique to a variety of problems. One of the first applications of the method involved the study of shock-wave structure

in a rigid sphere gas [52]. Density profiles were examined across the shock wave and the profiles compared favorably with continuum solutions. Comparison of the simulation procedures to the Boltzmann equation has been made by Bird [51]. It was shown that the simulation procedure retained the motion and collision processes described by the Boltzmann equation, but without requiring an explicit solution for the distribution function. Further studies of dissociating diatomic gases [53] and chemically reacting flows [54] have shown the versatility of the method when it was applied to complex gases.

The DSMC method has recently been used in the study of rarefied hypersonic flows [21,48-50]. In addition, results for the Space Shuttle Orbiter showed agreement with analysis in the continuum regime [21]. Departure occurred between the two methods in the transitional flow, but the DSMC results provided continuous and smooth flow gradients over a broad range of flow conditions even in the free molecular limit. Free molecular heat transfer and drag limits were reached in the low density studies, whereas continuum approaches did not provide meaningful results. Other related studies [48-50,55] are consistent in both the continuum limit and the collisionless free molecular limit. Experimental data validate the numerical simulation and the results, at the two limits, are encouraging [56-59].

## 2.2 Cell Criteria

A typical computational domain is depicted in Fig. 2.1. This domain consists of one or more arbitrary regions which are further subdivided into quadrilateral cells. The cells are the smallest computational units and provide a convenient reference for the sampling of the macroscopic gas properties. The dimensions of the cells are such



that the relative change in flow properties across each cell is small.

Binary collisions are the basis for the construction of the collision model and place requirements in the sizing of the cell network, estimation of the molecule transit time and population of the individual species in each cell. The first requirement is that the cell length in any direction be less than the mean distance between successive collisions.\* For cell lengths less than a mean free path, the likelihood of a collision in a single time increment is small, thus binary collisions (an assumption required for dilute gas theory) dominate as the collision mechanism. The cell dimensions in different directions may vary significantly because of density and velocity gradients. In a hypersonic gas flow, gradients are large in the surface normal directions compared to the flow direction which implies more collisions through viscous interaction. To capture these gradients, the cell density must be high near bounding surfaces and individual cells can increase in overall size as they are placed farther away from the body. Typically, lateral cell dimensions are specified as approximately one third the length of the smallest local mean free path in the vicinity of the cell.

The second requirement is the assignment of an appropriate time step for each computational cell. To insure that particles undergo the appropriate number of collisions as they traverse the flow domain, time is advanced in discrete intervals that are small in comparison with the mean collision time. Initial estimates of the time steps are made by dividing the cell dimensions by their corresponding parallel velocity

---

\*In a high velocity flow, the mean distance between successive collisions measured in the flow direction is much greater than the mean distance between successive collisions orthogonal to the flow direction.

components yielding an average transit time through the cell. Some fraction of this value is assigned as the time step for that cell.

A final consideration addresses the method by which statistical data are provided through molecule occupation numbers in each cell. To correctly model flow phenomena, many particles--each with their own chemical identity--must be present in each cell during physically important time intervals. Statistical data from these particles (such as velocity and energy) provide flowfield information required by the aerodynamist (such as pressure and temperature). A large cell occupation number reduces the statistical fluctuations caused by the averaging process (which are inversely proportional to the square root of the sample size). Statistical data can be obtained in one of two ways. One way is to average small cell populations over many time intervals. This is computationally demanding and greatly lengthens the time of a numerical simulation. The second approach is to employ large cell populations over a few time intervals to provide (in the limit of a large sample size) a statistically identical average. The benefit of this approach is realized in a smaller required computational time for the evolution of the solution. However, the larger particle population in the flow domain requires additional computer memory and management during the motion and collision simulation processes.

Gas flows involving multiple species may require large cell populations. As an example, consider air as a five species gas composed of  $N_2$ ,  $O_2$ , N, O and NO. Large numbers of  $N_2$  and  $O_2$  particles result when an effort is made to include nonzero contributions in the less abundant monatomic species. To represent correctly the specie number densities, several particles of a specie must be present in the cell. To maintain



the relative abundance of a five specie air model, a nominal minimum value of 30 particles per cell are maintained to assure representation of the least abundant molecule. That requirement results in large numbers of model particles representing the more abundant species in each cell. It should be noted here that, although it is desirable for each specie to be sampled in every cell, only cells near the bounding surfaces are of primary interest to the aerodynamist.

## 2.3 Equations and Processes

### 2.3.1 Cell population and molecular motion

Computations are generally initiated in a domain filled with particles resembling a freestream gas with particle energies representing a Maxwellian distribution. These particles are considered to be in thermal equilibrium. All particles are moved through distances appropriate to their velocity components and local time steps. New particles are introduced at input boundaries and are removed when a particle trajectory intercepts an exit boundary. Particles are inserted by sampling from a flux distribution function at the boundaries. They are positioned at the boundary randomly, and are monitored as they move through the flow domain. Collisions with a body surface result in either a diffuse or specular reflection. After particle movement, a set of representative collisions appropriate to the local time step is computed.

### 2.3.2 Collision Analysis

An accurate description of molecular collisions must include some statement about the functional dependence of cross-section on collision energy. The Variable Hard Sphere cross-section,  $\sigma_T$ , varies with the relative speed according to [60]:

$$\sigma_T \propto C_r^{-2\omega} \quad (2.1)$$

This cross-section is used to evaluate the frequency of collisions in the flowfield. Recall that the mean free path was defined as the characteristic distance between successive collisions. The mean free time is the average time interval between collisions and the reciprocal of this mean time interval (collision frequency,  $\nu$ ) is equal to the number of collisions per unit time. An evaluation of the collision frequency [51] can be obtained by considering the introduction of a test particle in a set of stationary target particles as shown in Fig. 2.2. If the test particle moves at a mean relative speed,  $C_r$ , in the gas, it collides with target particles within a volume swept through at a rate of  $C_r$  times the collision cross-section. For  $N$  particles in a given unit volume, the total number of collisions per unit time is given by the volume rate times the number density,  $n$ :

$$\nu = n\sigma_T C_r \quad (2.2)$$

It is essential for the collision model to faithfully represent the physics. This is achieved by providing a sufficient number of collisions for each computational time step. The number of collisions per unit time per unit volume is the collision frequency times the number density and is given by the equation:

$$N_c = \nu n / 2 = \sigma_T n^2 C_r / 2 \quad (2.3)$$

where the 1/2 is introduced because summing over all collisions involves counting each particle twice. If computational particles are used, each computational particle represents a prescribed number of physical particles--say  $F_{num}$ . This can be written as:

$$N_c = dN/(dt \cdot dV) = (1/2)(F_{num} N_m/dV)(n\sigma_T C_r) \quad (2.4)$$

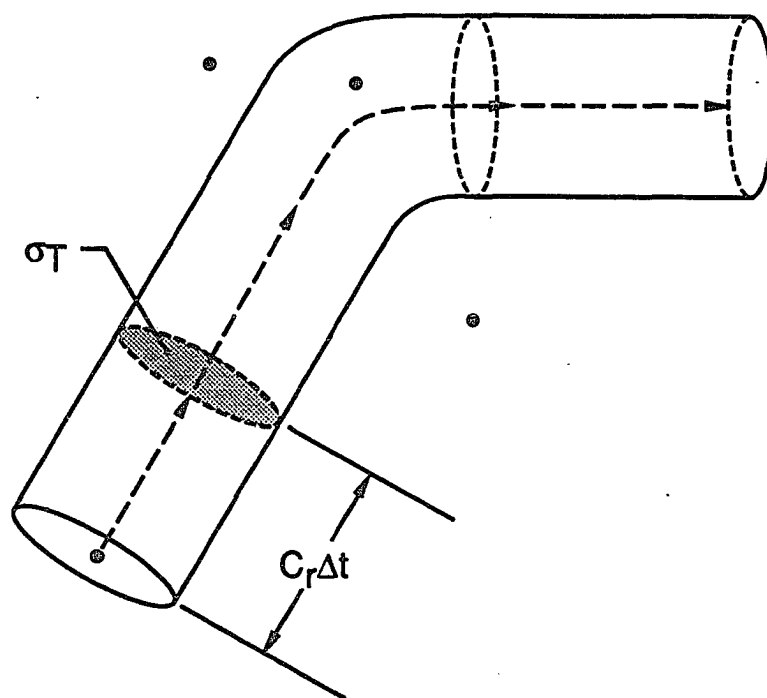


Figure 2.2 Test particle in a stationary gas.

where  $F_{\text{num}}$  is the number of physical particles represented by a computational particle,  $N_m$  is the number of simulated particles and  $V$  is the volume. This is further reduced to:

$$dN/dt = (1/2)(F_{\text{num}}N_m)n\sigma_T C_r \quad (2.5)$$

and for a single collision ( $dN = 1$ ):

$$dt_c = dt = 2/(F_{\text{num}}N_m\sigma_T C_r n) \quad (2.6)$$

where  $dt_c$  is the time increment added to the flow time for a single collision. Equation (2.6) indicates that  $dt_c$  is essentially proportional to the inverse square of the number of particles in a cell. As the number of computational particles in a cell increases, the increment  $dt_c$  decreases. Each collision results in an increment,  $dt_c$ , added to the cell clock to account for the effect of the collision pair upon the flowfield.

As noted earlier, the computational time step  $dt_m$  must be smaller than the average transit time of a particle through a computational cell. The transit time through the cell is given by the length of the cell side divided by the local average velocity of the gas and is governed by flow conditions and cell geometry. The minimum time resolution of the motion process is represented by  $dt_m$  which is assigned initially as an input variable and is adjusted as necessary until  $dt_m$  is less than the average cell transit time.

The minimum time resolution for the collision processes (as represented by  $dt_c$ ) can be thought of as the mean free time or the inverse of the collision frequency. To model the collision frequency correctly, particles in a cell must not leave the cell before being evaluated by the collision routine. If  $dt_m$  is much larger than the transit time, particles may move through a distance that includes several cells before

evaluation of the collision process can take place.

### 2.3.3 Energy Partition

To account for internal energy transfer between particles, a phenomenological model was developed by Borgnakke and Larsen [61]. The model considers binary collisions in a gas mixture with molecules which have an internal energy distribution. It is based on the relaxation of internal degrees of freedom such that a fraction of the molecular collisions are inelastic where energy is redistributed among the translational and internal degrees of freedom. New values of the internal and translational energies are generated by sampling randomly from the distribution functions for these quantities. The distribution functions correspond to those for an equilibrium gas at the prescribed conditions and the procedure requires conservation of energy and momentum. The remainder of the collisions are regarded as completely elastic and are treated classically as hard spheres which exchange only translational energy. Since the method is a statistical approach to energy partition, it is well suited to analyses that require particle descriptions. The Larsen-Borgnakke method [61] satisfies the principle of detailed balancing so that the effective temperatures associated with each energy mode approaches some mean equilibrium value.

The number of collisions required to equilibrate the population is provided by a characteristic collision number for the rotational and vibrational relaxation for each species involved. These empirical values [26,41,62] are equated to the reciprocal of the fraction of inelastic collisions. Using that relation to control the distributions, a random sampling can duplicate the appropriate relaxation rates. Energy exchange for inelastic collisions is controlled by examining the

total available collision energy, which is the sum of the relative kinetic energy of the colliding pair and of their respective internal energies. The energy is redistributed between the colliding pair using an equilibrium distribution function from which the post-collision translational energy is determined via random sampling. The remaining energy is reallocated to the various internal degrees of freedom of the participating particles. Monatomic particles play no part in the distribution of internal energy. For identical, internally active particles, the energy is, on the average, distributed uniformly between the pair. If, however, different species are involved, a distribution function which accounts for dissimilar internal degrees of freedom is sampled. From this sampling, assignments of energy to the rotational and vibrational modes for each particle are made.

#### 2.3.4 Chemistry

Chemical reactions are considered in the computational model if a collision between two reactive species takes place and their relative collision energy (translational energy along the line of particle centers) exceeds the activation energy. The simulated collision process provides the opportunity for energy transfer to occur, as required by a chemical reaction, but chemistry cannot occur unless sufficient energy is available for the reaction. Furthermore, physical particles in physical space (with the required energy) do not always react due to their orientation at the time of collision. Some method is required to monitor the collision energy and provide a probability for those collisions which are sufficiently energetic to result in a reaction.

Reactions are modeled in the DSMC method through the use of an integral reaction rate equation to create a reaction probability (or

steric factor) which is the ratio of the reactive cross-section to the total collision cross-section. This approach has been described by Bird [54] and employs the Boltzmann energy distribution for an equilibrium gas. The distribution function is substituted into the reaction rate equation and is integrated over all energy levels exceeding the activation energy. This integrated energy distribution function incorporates the energy of the colliding pair. The relation is further normalized by the collision cross-section, and the result yields a reaction probability for collisions that exceed the activation energy.

### 2.3.5 Catalytic Wall

The DSMC method can model a wall that is fully-, finite- or non-catalytic. A catalytic wall promotes recombination of flowfield species that undergo dissociation.

A wall that is catalytic is able to convert the translational and internal energy of colliding particles into energy available at the surface. This energy can be utilized in several ways. By way of illustration, consider flight conditions where  $N_2$ ,  $O_2$ ,  $N$ ,  $O$  and  $NO$  are present in the freestream and where  $N$  and  $O$  atoms dominate at the catalytic surface. An incoming  $O$  atom can provide sufficient energy to increase the thermal vibration of a wall particle such that the bond energy holding the particle to the wall is exceeded. The net result is the release of an  $O$  or  $N$  particle and the energy of the incoming atom can cause a chemical reaction at the wall resulting in the creation of an  $O_2$  or  $NO$  particle.

By specifying the degree of wall catalicity, the degree of wall

reactivity can be formulated. For a fully catalytic wall, the model assumes that all incoming monatomic oxygen and nitrogen species are recombined into their diatomic equivalent (as soon as the appropriate atomic partner is available). It should be noted that a catalytic surface is, in all likelihood, physically coated with N and O species and partners for recombination are readily available. Thus, the assumption of recombination upon collision with the surface is consistent with the physical surface.

A finite-catalytic wall condition uses a probability of recombination for each specie that is based on the wall temperature. Non-catalytic wall conditions assume that no recombination occurs at the wall.

## 2.4 Numerical Inputs

The DSMC method employs first principles, using data inputs at the molecular level. In fact, number density and boundary input flux are the only macroscopic parameters used. Particle specification includes molecular mass and diameter. The reference diameter is based on a hard sphere model at a given reference temperature but molecular diameter varies with temperature through the VHS model described earlier. The rotational degrees of freedom are zero and two for monatomic and diatomic particles, respectively. The characteristic vibrational temperature is required in the internal energy transfer process during the collision simulations. Estimates for rotational and vibrational relaxation can be developed in terms of the number of collisions required for complete adjustment to the equilibrium state. Nominal values of 5 and 50 collisions [63-65] are used for rotational and vibrational relaxation, respectively. For surface catalysis, only two



parameters are required: (1) the energy input to the surface due to recombination reactions and (2) the probability of a surface recombination reaction.

To describe the chemical processes during a reaction, several additional parameters are required. The number of contributing internal degrees of freedom for a reaction must be specified based on the species and type of reaction. The chemical reaction rates are incorporated as chemical cross-sections and consist of the three empirical constants used in the reaction rate equation. A final empirical input is required for the power law temperature exponent,  $\omega$ , used in the determination of the collision cross-section,  $\sigma_T$ . The exponent was developed by examining tables of temperature dependent viscosity data for each species considered and subsequently choosing a single value of  $\omega$  as the best curve fit for the mixture viscosity. The restriction of maintaining a single value of  $\omega$  is common to all previous phenomenological methods and represents the most serious limitation in engineering simulations.

## 2.5 Computational Considerations in the Use of DSMC

Since the DSMC method is a numerically intensive computer simulation, both computer memory capacity and central processing unit (CPU) speed are important considerations in the determination of an acceptable system. Memory requirements are related directly to the number of computational particles in the flow domain and to the number of cells required to capture flow gradients as dictated by the cell criteria mentioned earlier. To resolve flow gradients adequately, neighboring cell centroids must be sufficiently close to cause flow parameters to change by only a few percent. Some problems with sharp

gradients require a large number of cells (1000 or more) with 30 model particles per cell. In addition, the location, velocity and internal states of the 30,000 particles, along with empirical inputs and other flowfield information, must be retained in computer main memory. Computer storage demand increases in direct proportion to the number of particles and a typical main memory requirement for problems considered here is on the order of two megabytes.

The other consideration is the speed of the computations since the numerical simulation requires thousands of increments in time before achieving a steady state. Once having reached this point, an additional 1000 increments in the flow time are required to build up a sufficient number of samples in the flowfield parameters to enable statistical sampling. Typical problems generate 10 million collisions and 50 thousand chemical reactions at the particle level. Flow times are prescribed so that the gas has moved several body lengths in distance before the solution is allowed to build up statistical samples. Total flow times of milliseconds are nominally required for a meaningful sample size. To achieve this requirement a "fast" CPU is required.

The computational requirements were met by a Perkin-Elmer 3250 processor. This machine has a clock speed on the order of 150 nanoseconds (or an upper computational limit of 6.67 million instructions per second (MIPS)). The measured (benchmark) instruction execution rate is approximately 2.3 MIPS. This configuration of memory and clock speed translated into a simulation time requirement on the order of two weeks for a typical numerical experiment.

## Chapter 3

### PROBLEM FORMULATION

#### 3.1 Computational Code

##### 3.1.1 General Comments

The Direct Simulation Monte Carlo method provides a numerical simulation of a real gas by modeling the flow with some thousands of computational particles. This is achieved through the construction of the initialization, execution and output programs which provide a complete description of the numerical problem. Each program is tailored to the computational demands of the simulation and the execution sequence is shown schematically in Fig. 3.1 which can serve as a guide for the discussion which follows. Though it is not the intent of this work to report a line-by-line explanation of the computation codes, comments are necessary to illustrate the numerical simulation.

##### 3.1.2 Initialization Process

The initialization program reads a data file that contains the flowfield and solid surface information. Density, velocity, specie concentration and temperature are required for the flowfield description. Temperature, accommodation coefficient and a gas surface interaction model (diffuse, specular or a combination of both) are required in the description of all solid surfaces. A second set of data are required to provide a description of the computation domain which is

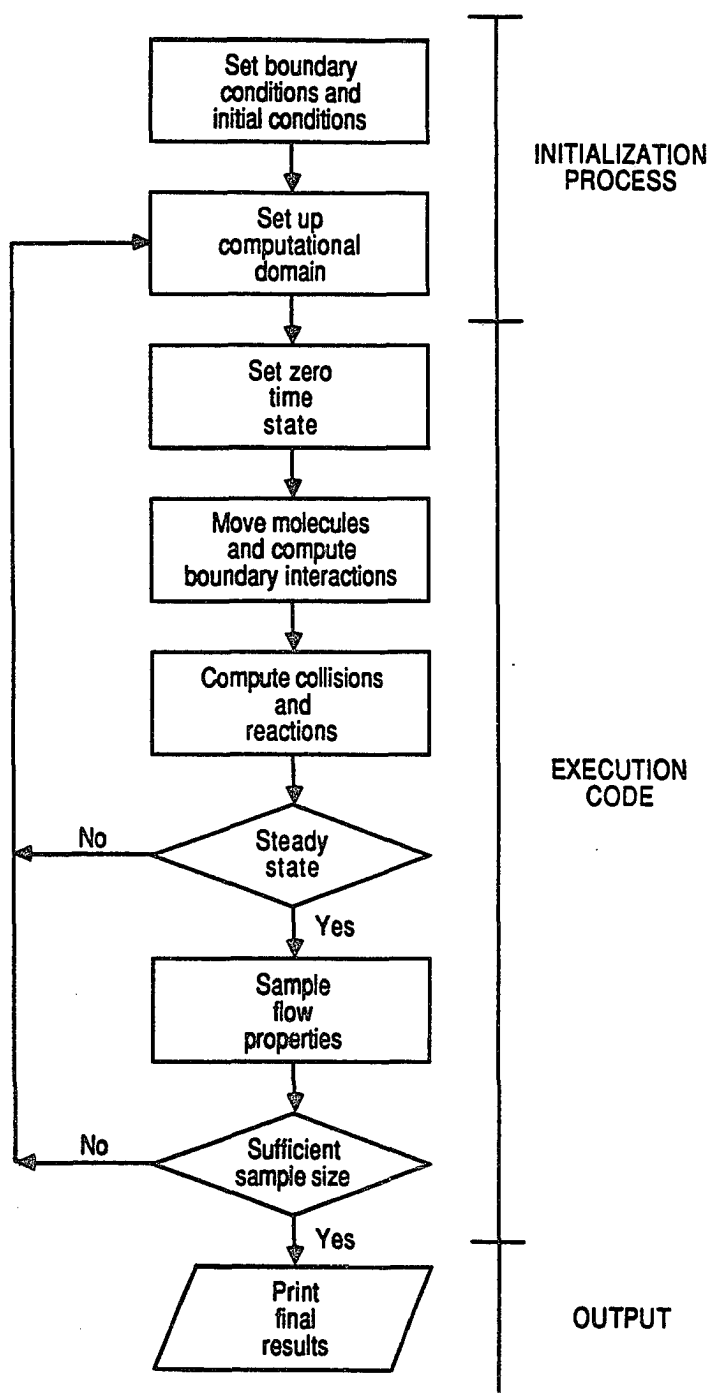


Figure 3.1 Flow chart of the computational code.

divided up into regions. The region corners are assigned locations in physical space and the corners are connected with polygonal line segments. The domain boundary description is followed by assignment of boundary conditions to the regional line segments. Vacuum, freestream, line of symmetry, hardware surface, axis or adjoining region surface are nominal choices. The region is then filled with quadrilateral cells according to prescribed inputs. Each cell is assigned an initial particle population (except those with no particles in the case of a vacuum condition) and represents the undisturbed freestream population expected for a similar volume in physical space. An additional variable associated with scaling from physical space to the model domain is required for each region. This parameter ( $F_{num}$ ) represents the number of physical particles associated with each computational particle. These assignments change from region to region but flux quantities that cross region boundaries are conserved (see Appendix A).

Geometry and flowfield data provided by input files and the initialization code are stored in large common block assignments (1 megabyte and larger). These files are stored in disk memory and are available upon demand for use in the execution and output codes.

### 3.1.3 Execution Code

The description of the computational domain is followed by the execution code. The first task of this program is to set up data blocks in computer main memory and retrieve the data files stored in disk memory. The program moves the computational particles through physical space appropriate to their local time step. The location of the particles after motion is recorded and particles that hit bounding surfaces are reflected. Particles that leave the computation domain are

discarded. For each time step, additional particles are introduced at input flux boundaries and correspond to the flux crossing a flowfield boundary from the undisturbed freestream. After particle motion, the number of representative collisions consistent with the motion increment is computed for each cell in the computational domain. Since each cell may contain a variety of molecular species, and these species vary in concentration, the collision routine chooses at random a pair of particles based on their respective probability of occurrence. The selection of potential collision pairs corresponds (on the average) to the same random selection if two particles are chosen in the real gas (species with a high concentration are chosen more often than those with a low concentration). If the relative velocity between a possible collision pair is sufficiently large that the pair passes an acceptance-rejection test, a collision occurs. The pairs are evaluated using random numbers to determine if a collision occurred. Chemical and energy transfer processes are evaluated only after a collision. An increment in the cell time is made for each pair of particles that collide. It is based on the collision that just occurred and the numerical value of  $dt_c$  is computed for each collision. When the cell collision time exceeds the flow time, collisions in that cell are complete and a new cell is processed through the collision routine. Computation of the collision process is complete when all local cell times are incremented to the current flow time.

If the flow time is less than the time required to achieve steady state, the arrays that contain the cumulative total sample of the flow-field parameters are reset to zero. If steady state is achieved, the sampling procedure is begun and cumulative totals of the flow parameters

are built up as the program moves particles and computes collisions. Statistical data on the modeled molecules (by specie) ( $\Sigma u$ ,  $\Sigma v$ ,  $\Sigma w$ ,  $\Sigma u^2$ ,  $\Sigma v^2$ ,  $\Sigma w^2$ ,  $\Sigma e_{\text{rot}}$  and  $\Sigma e_{\text{vib}}$ ) are accumulated by sampling these statistical quantities at prescribed flow times. From these statistical data, the physical flow properties are computed by the output code. These values are stored for further use. This procedure is continued until the prescribed number of samples is obtained.

#### 3.1.4 Output Code

The output code utilizes the cell information that is averaged over a given number of samples. Large samples of a thousand or more (as required to reduce statistical fluctuations) provide output of pressure, shear stress, density and heat flux quantities on surface elements and temperature, density, velocity and energy in the flowfield. Typical forms of the data provided in this thesis include density, velocity and temperature along the stagnation streamline and over the bounding surfaces. Body normal profiles and contour plots are also included to yield insight into the physical behavior of the flowfield.

### 3.2 Numerical Inputs for Current Study

The problem formulation incorporated a five species ( $N_2$ ,  $O_2$ ,  $N$ ,  $O$ ,  $NO$ ) gas to represent air over a range of altitudes (70 to 100 km) encountered by a reentry vehicle. The abundant molecules ( $N_2$ ,  $O_2$ ) and their products ( $N$ ,  $O$  and  $NO$ ) were a convenient set when considering chemical reactions. Species with low concentration in the freestream ( $CO$ ,  $Ar$ , ions and electrons) were not considered because their inclusion would not alter the pressure and heating rate significantly. Gaseous, radiation heat-transfer was not considered in the present study. Inclusion of a particle by particle radiation model would increase the

computational requirements significantly because of molecular absorption, scattering and re-radiation. However, radiation was neglected primarily on the basis that the effects on the flowfield of a shuttle reentry vehicle at speeds of 10 km/s were minor [66]. The current study has considered much smaller objects at lower flight velocities and, therefore, the inclusion of radiation effects is not justified.

For the five species model, 34 reactions can be identified which represent all probable reactions expected for the species set. Reaction rates were provided by Bortner [67]. The rates were provided by a reaction rate equation in the form:

$$K(T) = aT^b \exp(E_a/kT) \quad (3.1)$$

where  $a$  and  $b$  are constants,  $E_a$  is the activation energy,  $k$  is the Boltzmann constant and  $T$  is the temperature. Bortner's constants for the 34 reactions are tabulated in Table 3.1. Most of the data developed by Bortner [67] were inferred from experiments with gases in a state of thermodynamic equilibrium at moderate temperatures (ambient to 1000 K). Thermal nonequilibrium recovery rates and reaction rates above 1500 K are uncertain. Obviously, nonequilibrium data are difficult to obtain experimentally at any temperature. Until data are provided at high temperature conditions, there appears to be no alternative but to use low energy equilibrium data for high energy thermodynamic nonequilibrium conditions. It should be noted further that the number of empirically derived constants which have been introduced through the 34 reactions tends to obscure the high energy effects anyway.

Recombination probabilities appropriate for the surfaces of the blunt bodies require definition of the actual surface material. The



TABLE 3.1 REACTION RATE COEFFICIENTS

Reaction	a (m <sup>3</sup> /molecules·s)	b	E <sub>a</sub> (Joules)
1 O <sub>2</sub> + N → 2O + N	5.993 x 10 <sup>-12</sup>	-1	8.197 x 10 <sup>-19</sup>
2 O <sub>2</sub> + NO → 2O + NO	5.993 x 10 <sup>-12</sup>	-1	8.197 x 10 <sup>-19</sup>
3 O <sub>2</sub> + N <sub>2</sub> → 2O + N <sub>2</sub>	1.198 x 10 <sup>-11</sup>	-1	8.197 x 10 <sup>-19</sup>
4 2O <sub>2</sub> → 2O + O <sub>2</sub>	5.393 x 10 <sup>-11</sup>	-1	8.197 x 10 <sup>-19</sup>
5 O <sub>2</sub> + O → 3O	1.498 x 10 <sup>-10</sup>	-1	8.197 x 10 <sup>-19</sup>
6 N <sub>2</sub> + O → 2N + O	3.187 x 10 <sup>-13</sup>	-0.5	1.561 x 10 <sup>-18</sup>
7 N <sub>2</sub> + O → 2N + O <sub>2</sub>	3.187 x 10 <sup>-13</sup>	-0.5	1.561 x 10 <sup>-18</sup>
8 N <sub>2</sub> + NO → 2N + NO	3.187 x 10 <sup>-13</sup>	-0.5	1.561 x 10 <sup>-18</sup>
9 2N <sub>2</sub> → 2N + N <sub>2</sub>	7.968 x 10 <sup>-13</sup>	-0.5	1.561 x 10 <sup>-18</sup>
10 N <sub>2</sub> + N → 3N	6.9 x 10 <sup>-8</sup>	-1.5	1.561 x 10 <sup>-18</sup>
11 NO + N <sub>2</sub> → N + O + N <sub>2</sub>	6.59 x 10 <sup>-10</sup>	-1.5	1.043 x 10 <sup>-18</sup>
12 NO + O <sub>2</sub> → N + O + O <sub>2</sub>	6.59 x 10 <sup>-10</sup>	-1.5	1.043 x 10 <sup>-18</sup>
13 NO + NO → N + O + NO	1.318 x 10 <sup>-8</sup>	-1.5	1.043 x 10 <sup>-18</sup>
14 NO + O → N + O + O	1.318 x 10 <sup>-8</sup>	-1.5	1.043 x 10 <sup>-18</sup>

TABLE 3.1 CONCLUDED

	Reaction	a (m <sup>3</sup> /molecules·s)	b	E <sub>a</sub> (Joules)
15	NO <sub>2</sub> + N → 2N + O	1.318 x 10 <sup>-8</sup>	-1.5	1.043 x 10 <sup>-18</sup>
16	NO + O → O <sub>2</sub> + N	5.279 x 10 <sup>-21</sup>	1.0	2.719 x 10 <sup>-19</sup>
17	N <sub>2</sub> + O → NO + N	1.120 x 10 <sup>-16</sup>	0	5.175 x 10 <sup>-19</sup>
18	O <sub>2</sub> + N → NO + O	1.598 x 10 <sup>-18</sup>	0.5	4.968 x 10 <sup>-20</sup>
19	NO + N → N <sub>2</sub> + O	2.49 x 10 <sup>-17</sup>	0	0
20	N + N + N → N <sub>2</sub> + N	6.3962 x 10 <sup>-40</sup>	-1.5	0
21*	O + O + M → O <sub>2</sub> + M	8.297 x 10 <sup>-45</sup>	-0.5	0
22*	N + N + M → N <sub>2</sub> + M	3.0051 x 10 <sup>-44</sup>	-0.5	0
23*	N + O + M → NO + M	2.7846 x 10 <sup>-40</sup>	-1.5	0

---

\*M is a Third Specie That Participates in the Reaction.

thermal protection tile (Shuttle tile) manufactured from a silica base material with a glass coating was used as the reference material surface in this study. Recombination rates for this material are available and are functionally dependent only upon the surface temperature. From Throckmorton [68], the surface temperature profiles during the first Shuttle reentry flight experiment indicated a range of surface temperatures from ambient to 1100 K. A nominal wall temperature of 1000 K was used for convenience in this study. From Zoby et al. [69], arcjet experimental data and Shuttle reentry data provided recombination rates for the temperature of interest. A recombination probability of 0.0077 was obtained for oxygen. Scott [19] provided arcjet experimental data and a recombination probability of 0.0049 was obtained for nitrogen at a wall temperature of 1000 K. Those values have been used in this study.

Collision cross-sections were provided by the following relation:

$$\sigma_T = \sigma_{\text{ref}} \left( \frac{T_{\text{ref}}}{T} \right)^{\omega-0.5} \quad (3.2)$$

where  $\sigma_{\text{ref}}$  is a reference collision cross-section at a given reference temperature  $T_{\text{ref}}$ . These reference values [70] were provided for a variety of species. By obtaining a value of viscosity at a given temperature  $T$ , the collision cross-section of the gas could be determined by the Chapman-Enskog relation [40]:

$$\mu = (15m/8) (\pi RT)^{1/2} / [2 - (\omega - 0.5)^{\omega-0.5} \Gamma(4 - \omega - 0.5) \sigma_T] \quad (3.3)$$

where  $\omega$  is the power law temperature exponent and  $\Gamma$  is the gamma function. Since collisions involved multiple species and only a single collision cross-section can be used at a time, the numerical simulation

required a single value for  $\omega$ . In effect, the five species (each governed by a separate value of  $\omega$ ) were represented by a single power law relation. Agreement with the dominant specie,  $N_2$ , served as a first approximation for the comparison of tabulated viscosity data with a single power law model. A one-to-one correspondence was found for  $N_2$  over the temperature range of 0 to 10,000 K, for an exponent of  $\omega = 0.730$ . Since this value only approximated the viscosity for the other species, the degree of departure was an important consideration. Diatomic oxygen, which is the next highest concentration of gas in the freestream experienced a 5% departure using that exponent over the 0 to 10,000 K temperature range. Similarly, departures of 4%, 2% and 18% were found for O, NO and N, respectively. While the error in N is large, the influence of chemical reaction (creation and annihilation of species) is probably larger, and there is presently no systematic method for including these effects.

Furthermore, the freestream gas at the altitudes studied are nearly void of N and NO species. They are important, statistically, only near the surface of the body. The inability to incorporate five power law models for viscosity is not as serious as it might be in other flow situations. The use of a single exponent was accepted as a reasonable compromise in this setup.

### 3.3 Geometry and Flow Conditions

The flowfield structure and the aerothermodynamic characteristics of blunt bodies under hypersonic transitional flow conditions are provided by a numerical study of flow about wedges and cones (see Fig. 2.1). Body half angles of  $0^\circ$ ,  $5^\circ$  and  $10^\circ$  for both configurations with a nose radius of 0.0254 m have been used to model the leading edges of

hypersonic vehicles currently under development. The altitude range considered was 70 to 100 km and the freestream velocity (nominal for shuttle reentry flight) is 7.5 km/s. Calculations accounted directly for translational, rotational, vibrational and chemical nonequilibrium effects using a 5 species ( $N_2$ ,  $O_2$ ,  $N$ ,  $O$  and  $NO$ ) gas model of air (see Table 3.2). Body surface temperature was assumed constant at 1000 K and the wall was considered diffuse with full thermal accommodation. The wall was assumed to be finite-catalytic in the sense that it was able to promote recombination of the oxygen and nitrogen atoms. For altitudes of 90 km, and above, the assumed freestream conditions were those given by Jacchia [71] for an exospheric temperature of 1200 K, whereas the conditions below 90 km are those given in the U.S. Standard Atmosphere [72]. These freestream conditions and other flowfield parameters and surface data are given in Tables 3.3 and 3.4.

### 3.4 Viscous Shock Layer Calculations

The continuum calculations presented for comparison purposes were obtained by solving the steady viscous shock-layer (VSL) equations. The VSL equations are obtained from the Navier-Stokes equations by keeping terms up to second order in the inverse square root Reynolds number, i.e.,

$$\epsilon = \sqrt{\mu_{\text{ref}} / \rho_{\infty} U_{\infty} R_N}$$

where  $\mu_{\text{ref}}$  is the reference viscosity evaluated at a reference temperature ( $T_{\text{ref}} = U_{\infty}^2 / C_p$  where  $C_p$  is the freestream specific heat). Consequently, one set of equations, uniformly valid throughout the shock layer, is solved for both the inviscid and viscous regions. The VSL results presented were obtained by Thompson [73] using the three-

TABLE 3.2 REPRESENTATIVE GAS PROPERTIES

Gas	Molecular Weight (kg/kmole)	Ratio of Specific Heats	Nominal Diameter (m)	Molecular Mass (kg)	Characteristic Vibrational Temperature (K)
N <sub>2</sub>	28.0	1.40	$3.083 \times 10^{-10}$	$4.65 \times 10^{-26}$	3390
N	14.0	1.67	$2.398 \times 10^{-10}$	$2.325 \times 10^{-26}$	-
O <sub>2</sub>	32.0	1.40	$3.062 \times 10^{-10}$	$5.31 \times 10^{-26}$	2270
O	16.0	1.67	$2.297 \times 10^{-10}$	$2.65 \times 10^{-26}$	-
NO	30.0	1.40	$3.065 \times 10^{-10}$	$4.98 \times 10^{-26}$	2740

Table 3.3 FREESTREAM CONDITIONS

Altitude, km	Density, kg/m <sup>3</sup>	$U_{\infty}$ km/s	$T_{\infty}$ K	Mole Fractions			$\bar{M}$ g/mol	$\lambda_{\infty}$ m
				$X_{O_2}$	$X_{N_2}$	$X_O$		
100	$5.641 \times 10^{-7}$	7.5	194	0.177	0.784	0.039	28.26	$1.37 \times 10^{-1}$
95	$1.396 \times 10^{-6}$	7.5	189	0.197	0.787	0.016	28.61	$5.59 \times 10^{-2}$
90	$3.418 \times 10^{-6}$	7.5	188	0.209	0.788	0.003	28.81	$2.30 \times 10^{-2}$
85	$7.955 \times 10^{-6}$	7.5	181	0.237	0.763	0	28.96	$9.94 \times 10^{-3}$
80	$1.999 \times 10^{-5}$	7.5	181	0.237	0.763	0	28.96	$3.96 \times 10^{-3}$
70	$8.753 \times 10^{-5}$	7.5	220	0.237	0.763	0	28.96	$9.03 \times 10^{-4}$

Table 3.4 FREESTREAM PARAMETERS AND SURFACE COEFFICIENTS

Altitude, km	$Re_{\infty}$	$Kn_{\infty}$	$K_f^2$	$S_{\infty}$	Stagnation Heat Flux, kW/M <sup>2</sup>			C	
					2-D	Axial	Plate	Wedge <sup>a</sup>	Cone <sup>a</sup>
100	8	5.38	0.05	22.2	102	114	1.29	1.01	1.91
95	21	2.20	0.11	22.6	235	-	1.29	-	-
90	52	0.91	0.28	22.8	511	595	1.22	0.85	1.52
85	125	0.39	0.64	23.3	928	1300	1.07	0.73	1.26
80	313	0.16	1.61	23.3	1451	2500	0.90	0.61	0.96
70	1159	0.04	7.05	21.1	1920	5353	-	-	-

<sup>a</sup> $\alpha_0 = 5$  deg

dimensional nonequilibrium method developed by Kim, Swaminathan, and Lewis [74] and later modified by Thompson [75].



## Chapter 4

### RESULTS AND DISCUSSION

Some of the results of this investigation have already appeared in the literature [76,77] because of the current interest in the problem. This is the first comprehensive summary of all of the results and no distinction will be made between the current and previously reported results since the work was all performed by this investigator.

Before proceeding with the presentation of results, it will be necessary to expand the discussion of Knudsen number. That discussion is needed to assist in identifying the various transitional, continuum and rarefied flow regimes.

#### 4.1 Knudsen Number

The variation of the local Knudsen number along the stagnation streamline is shown in Fig. 4.1 for the 70 and 80 km cases. Local Knudsen numbers are defined by the ratio of the local mean free path to the local characteristic length as defined by the density gradient:

$$1/\ell = (1/\rho) \, dp/dn \quad (4.1)$$

Variations in Knudsen number are evident, with large values near surfaces and shock waves. A suggested rule of thumb [47,78] is that the

continuum equations are not valid if the local Knudsen number exceeds a critical value of about 0.1. According to this criterion, a significant

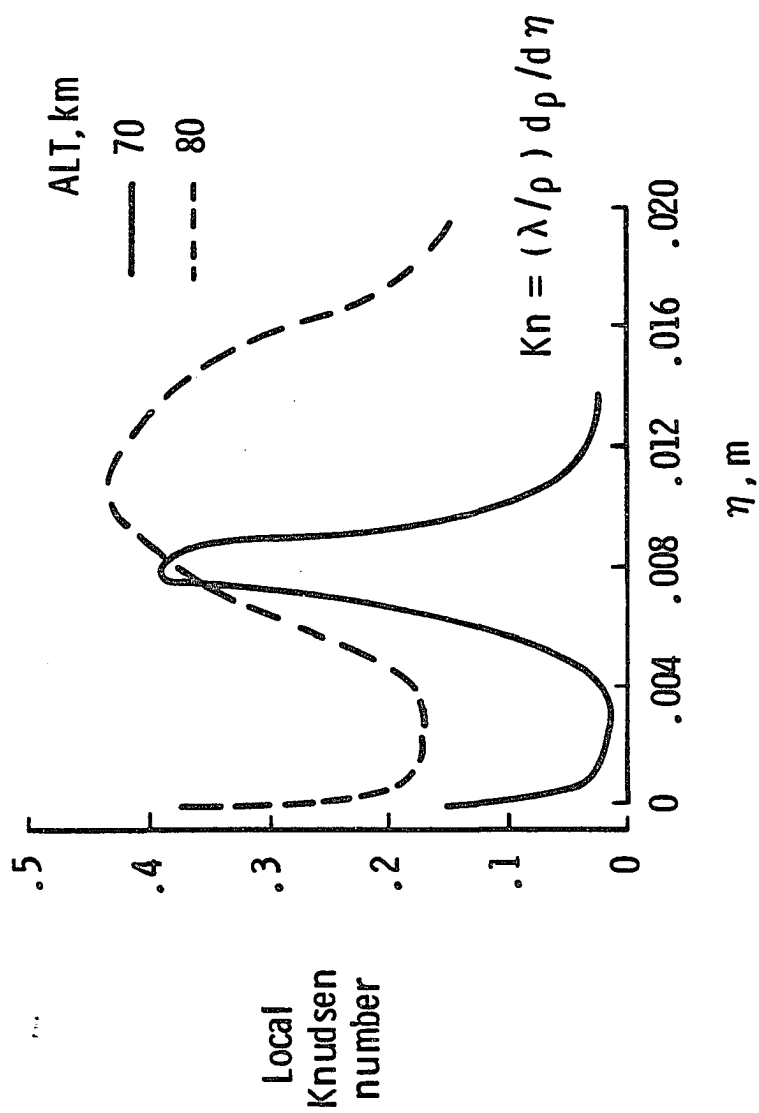


Figure 4.1 Local Knudsen number along the 2-D stagnation streamline.

part of the flow in the stagnation region, for the 80 km case, is modeled inappropriately using a continuum description.

#### 4.2 Two-Dimensional Flows

This section will focus on calculated results for the cylindrically blunted wedge with half angles of  $0^\circ$ ,  $5^\circ$  and  $10^\circ$ . Results at 70 and 85 km are emphasized to demonstrate and contrast differences in flow structure corresponding to the near continuum and the transitional flow conditions, respectively.

The two quantities in gas dynamic flows that are fundamental quantities independent of equilibrium conditions are number density and velocity. Other flow properties such as the temperature and pressure are inferred from the density and velocity and become imprecise according to the degree of nonequilibrium. The variation of density and velocity along the stagnation streamline and their dependence on rarefaction is demonstrated in Figs. 4.2 and 4.3 for altitudes between 70 and 90 km. Two regions of interest in the flowfield are near the wall and the shock wave. A large increase in density occurs near the wall and is characteristic of a cold-wall reentry condition. At 70 km, the stagnation density is more than two orders of magnitude greater than the freestream density. Profiles (unlike their continuum counterpart) are continuous and smooth through the shock wave, yet an inflection in the density profile becomes more pronounced for less rarefied conditions. The 70 km shock wave is of the same order of thickness as the shock layer indicating that the shock wave is merged with the shock layer.

The normal velocity profiles (Fig. 4.3) approach the freestream velocity of 7.5 km/s and show a more gradual merging of the shock layer

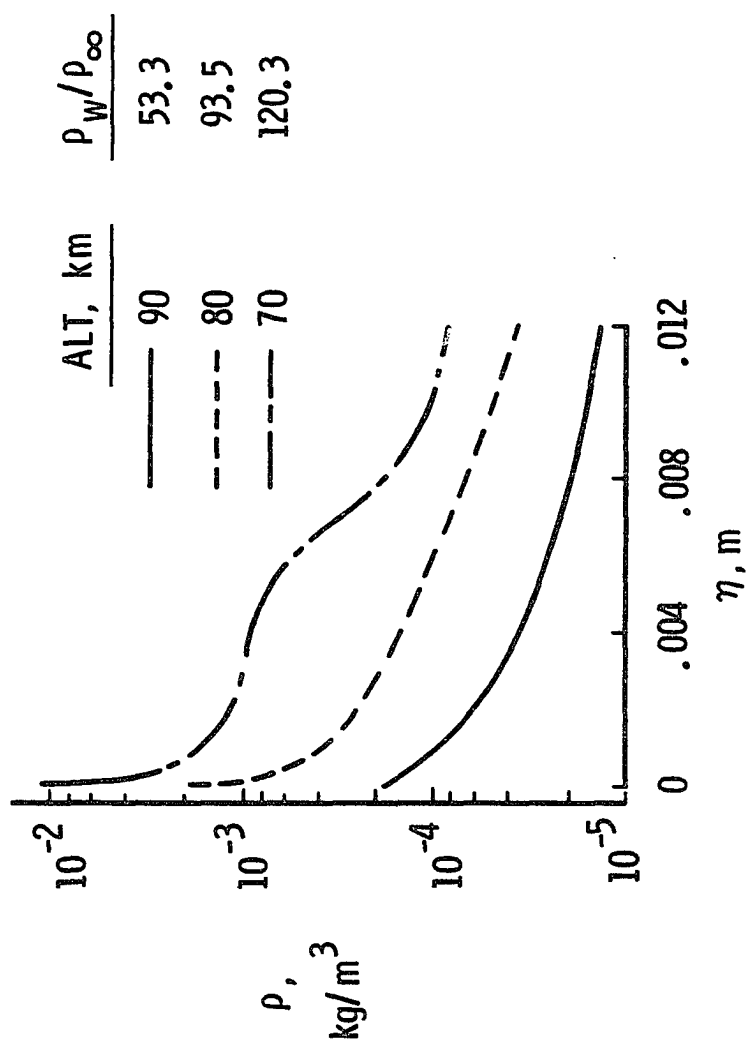


Figure 4.2 Effect of rarefaction upon the 2-D stagnation streamline density profiles.

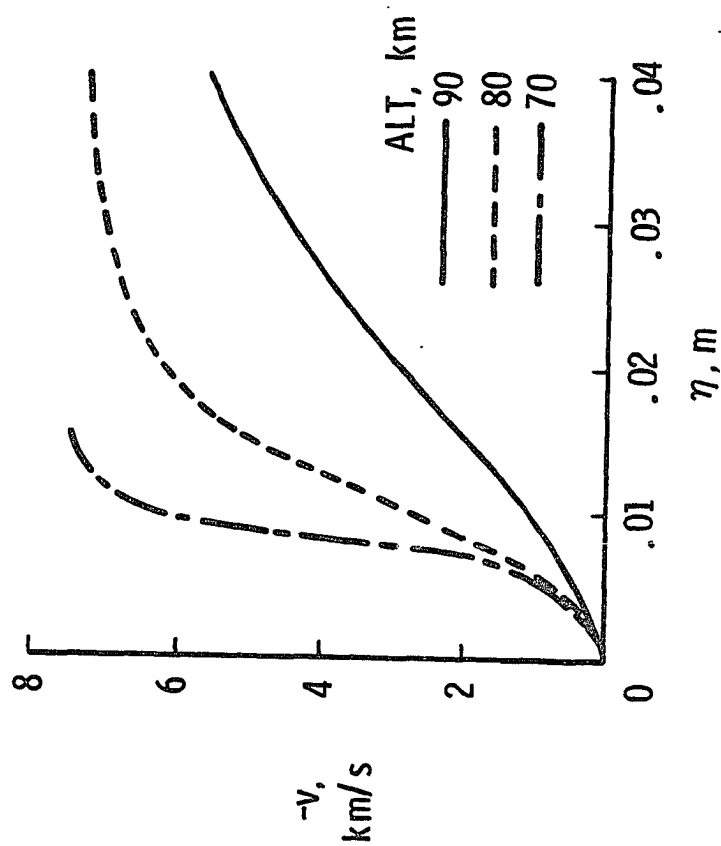


Figure 4.3 Effect of rarefaction upon the 2-D stagnation streamline normal velocity profiles.

and shock wave with increasing rarefaction. As a point of reference, the Rankine-Hugoniot relations give a post-shock velocity of 0.75 km/s, which corresponds to a small fraction of the total flowfield disturbance as predicated by the DSMC method.

The stagnation streamline temperature and species mass fraction profiles for the 70 km case are presented in Figs. 4.4 and 4.5, respectively. Thermodynamic nonequilibrium is evident throughout the shock wave and into the outer part of the shock layer as evidenced by the lack of equilibration of the translational and internal kinetic temperatures. The overall kinetic temperature (defined for the nonequilibrium gas as the weighted mean of the translational and internal temperatures (see Eq. 1.26 of Ref. 31) is not the same temperature as that defined by its ideal gas equation of state. Only under thermal equilibrium conditions, where the translational, rotational and vibrational temperatures are identical, is the overall kinetic temperature and the thermodynamic temperature equivalent.

The rapid translational kinetic temperature rise precedes the density rise (Fig. 4.2). For example, the translational kinetic temperature is a maximum at 10.76 cm from the surface while the density has increased by only a factor of 2.4. The initial translational kinetic temperature rise results from the essentially bimodal velocity distribution: the molecular sample consists of mostly undisturbed freestream molecules with just a few molecules that have been affected by the shock. The large velocity separation between these two classes of molecules give rise to early elevation of translational kinetic temperatures. The overall kinetic temperature disturbance extends about 2.5 nose radii upstream of the surface in the stagnation region (Fig.

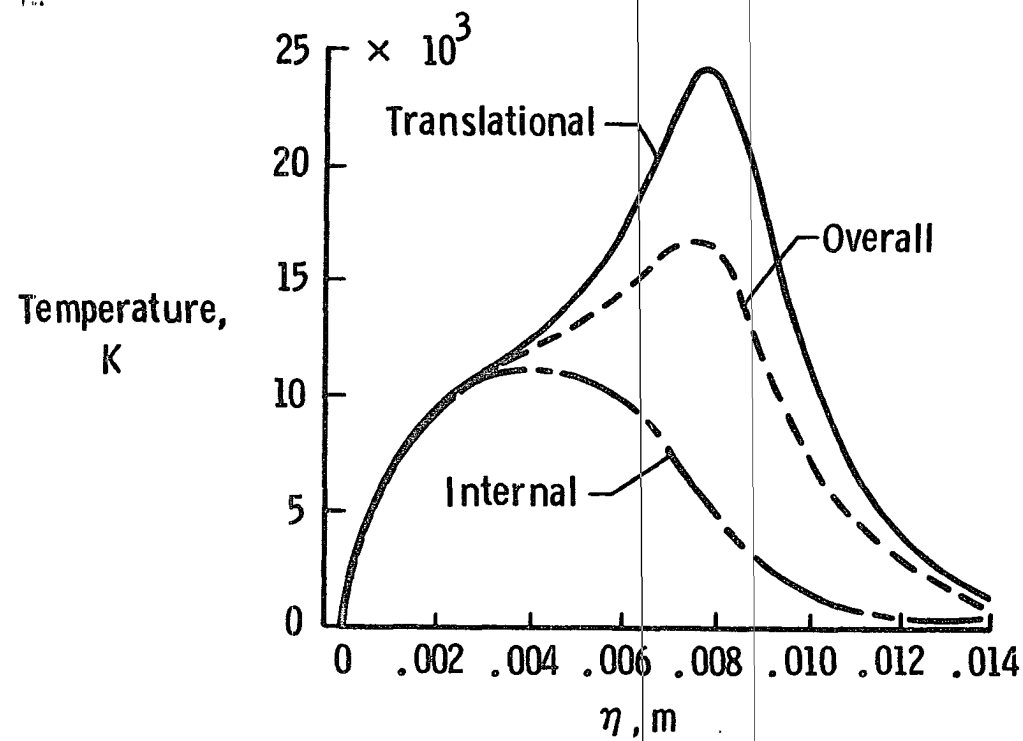


Figure 4.4 Extent of thermodynamic nonequilibrium along the 2-D, 70 km stagnation streamline.

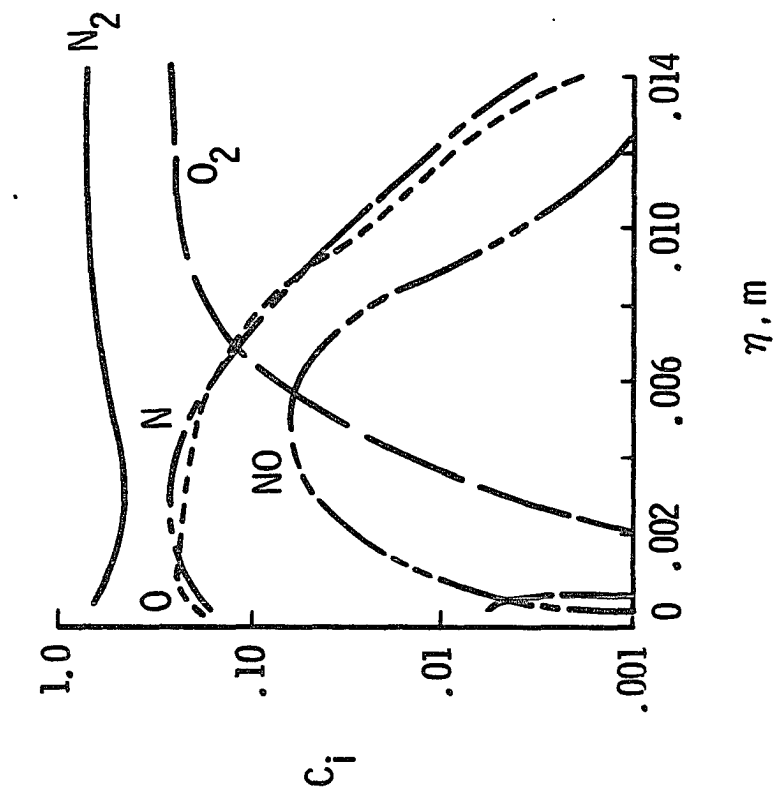


Figure 4.5 Species mass fractions along the 2-D, 70 km stagnation streamline.



4.6) and more than six nose radii away from the surface at an  $s/R_N$  location of eight. The conditions along the surface experience significant changes with the expansion to the downstream conditions: the stagnation density is 75 times freestream (not indicated in Fig. 4.7 since the density increases substantially near the surface) whereas the surface density near the end of the plate is only three times its freestream value.

Even though the gas is compressed significantly in the stagnation region, the kinetic temperature profiles along the stagnation streamline and near the surface (Fig. 4.8) show that thermodynamic equilibrium is not achieved. The energy associated with the translational and internal energy modes does not conform with the Boltzmann distribution where each energy mode has identical energies. The overall kinetic temperature of the gas adjacent to the surface is 1920 K and is almost twice the specified wall temperature. At a distance of about one local mean free path from the surface, the overall kinetic temperature is 3300 K and corresponds to the jump condition in continuum formulations [79]. The temperature jump values are greater at an  $s/R_N$  location of 4.1 (Fig. 4.9) where the overall kinetic temperature adjacent to the surface is 2252 K. Surface pressure and heat-transfer distributions expressed in coefficient form are presented in Figs. 4.10 and 4.11, respectively, for the cylindrically blunted portion of the flat plate. The effects of rarefaction are demonstrated by comparing the calculated results for 70, 85, and 100 km. The pressure coefficient data are bounded by the modified Newtonian and free-molecule values for most of the nose region. The variation of the pressure coefficient due to rarefaction effects is moderate provided the gas-surface interaction is diffuse, as assumed in

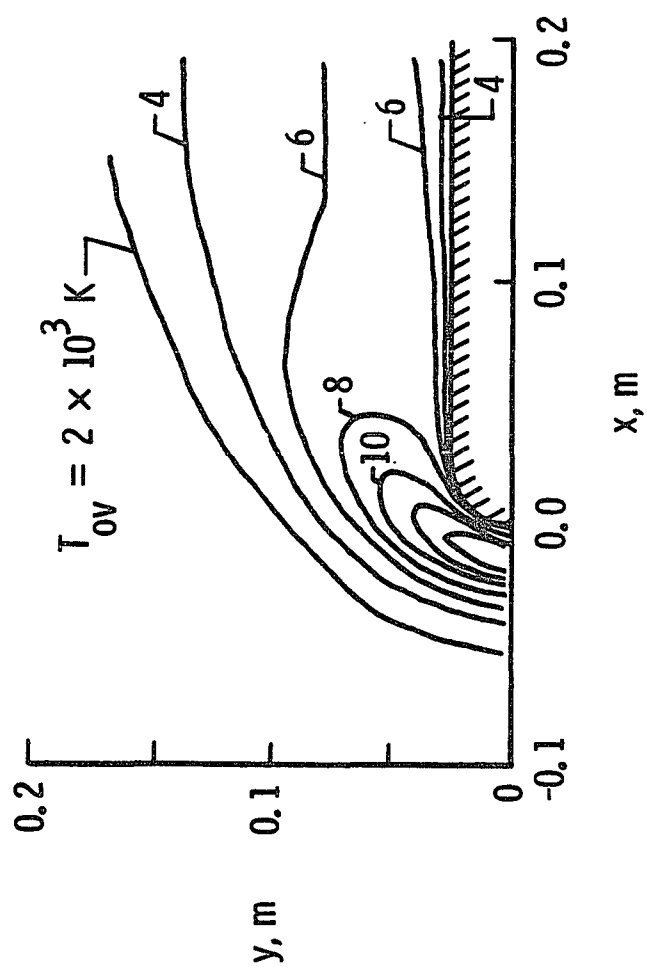


Figure 4.6 Overall kinetic temperature contours for the blunt flat plate at 85 km.

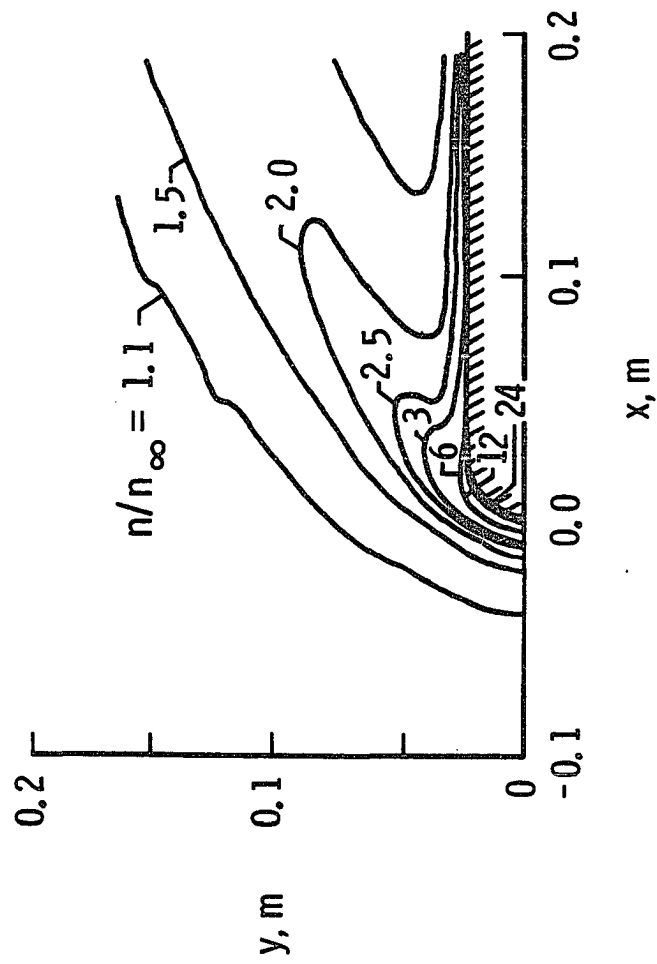


Figure 4.7 Number density contours for the blunt flat plate at 85 km  
( $n = 1.65 \times 10^{20} m^{-3}$ ).

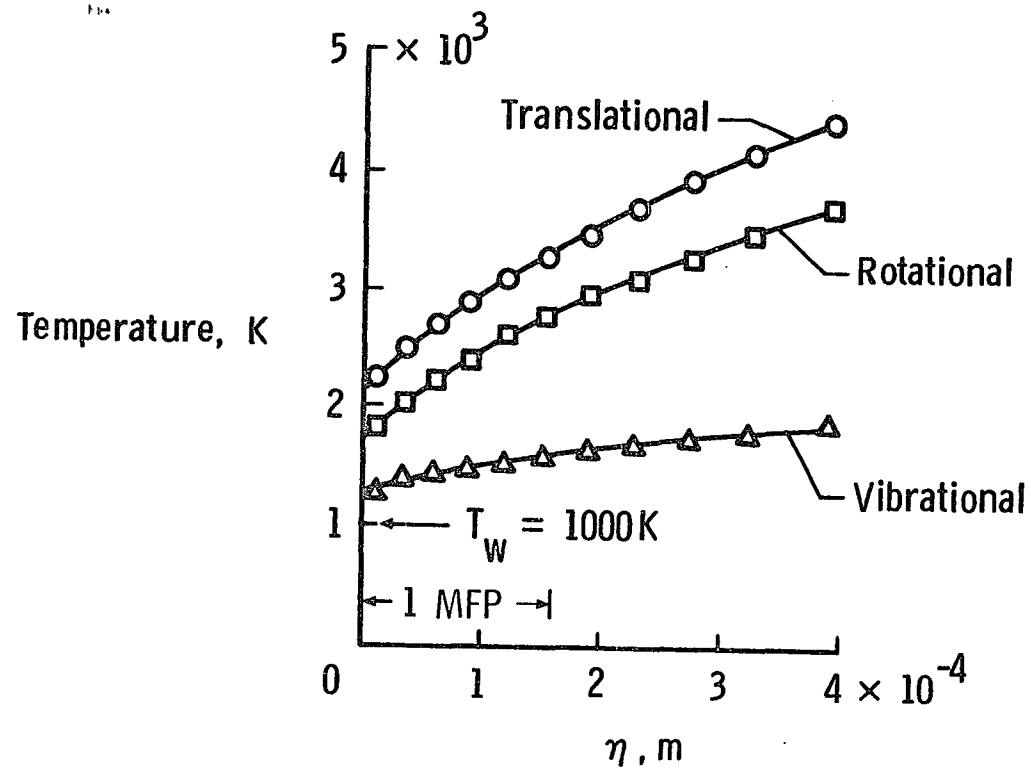


Figure 4.8 Temperatures adjacent to the blunt flat plate at 85 km,  $s/R_N = 0$ .

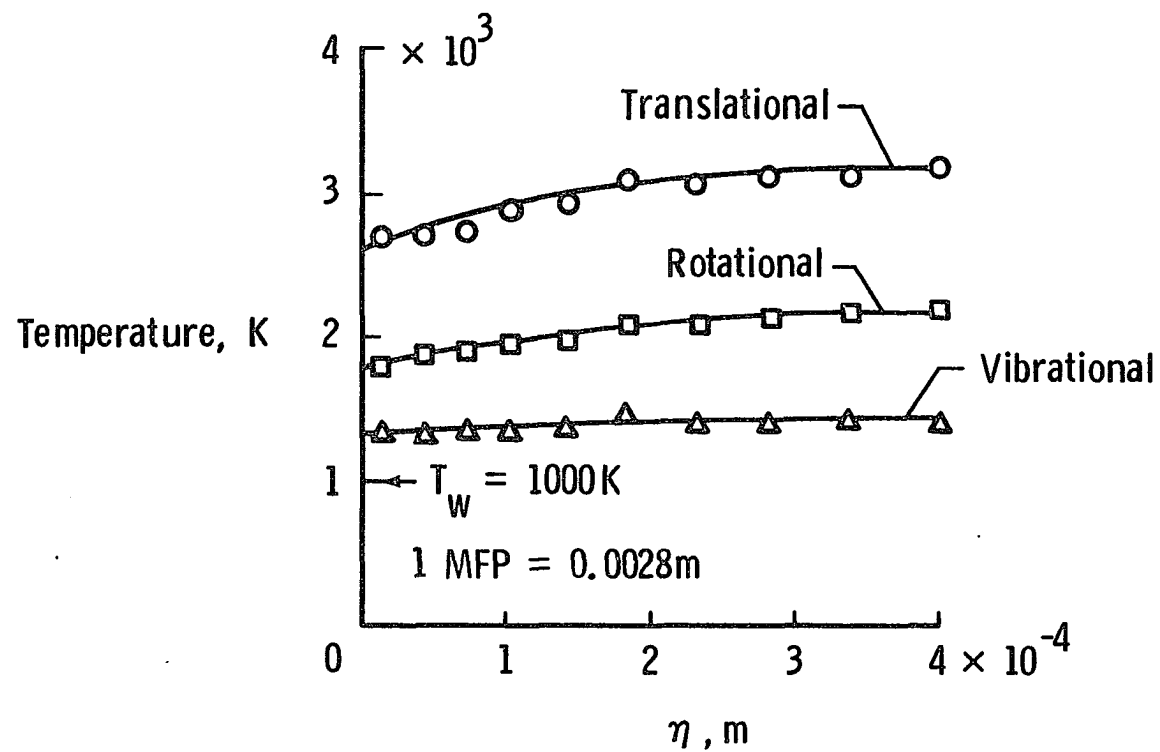


Figure 4.9 Temperatures adjacent to the blunt flat plate at 85 km,  $s/R_N = 4.1$ .

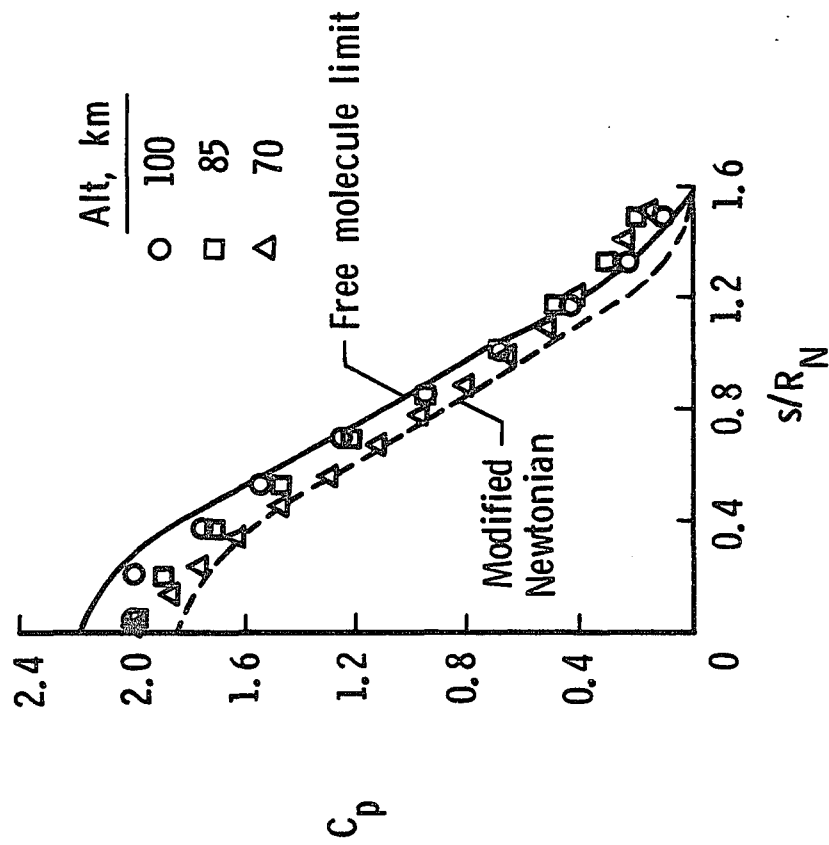


Figure 4.10 Effect of rarefaction on the 2-D wall pressure coefficient.

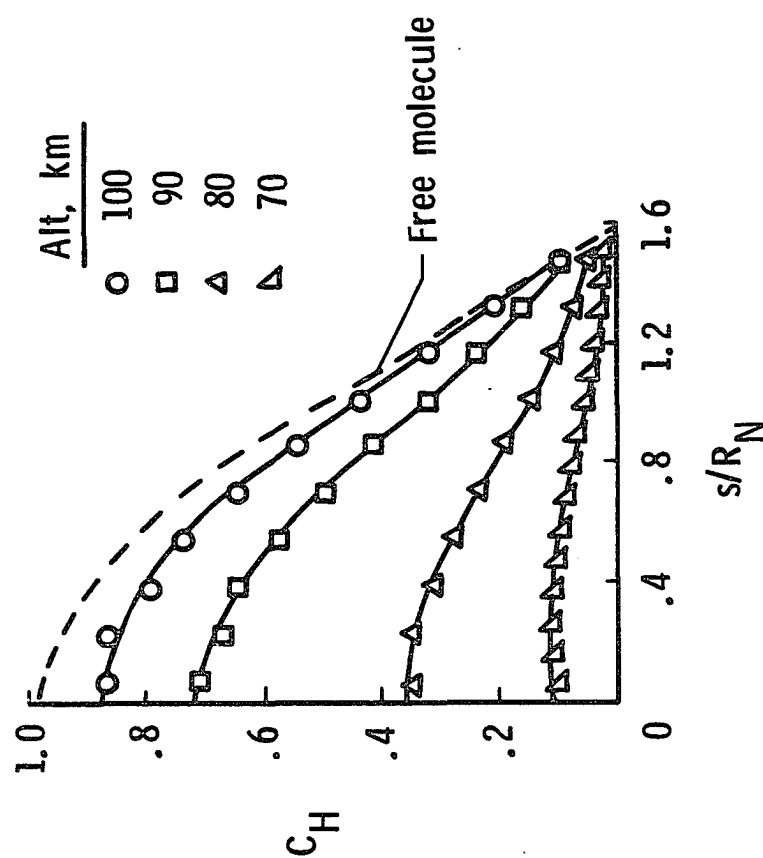


Figure 4.11 Effect of rarefaction on the 2-D heat-transfer coefficient.

the present calculations. In contrast, the heat-transfer coefficient (Fig. 4.11) is very sensitive to rarefaction effects, approaching the free molecule value with increasing rarefaction. As  $C_H$  increases to the free molecule limit atoms reach the surface with more kinetic energy than cases when  $C_H$  is small. This implies that the gas molecules are undergoing fewer molecular collisions as they approach the surface.

For the 85 km condition, calculations are provided for wedge half angles of  $0^\circ$ ,  $5^\circ$  and  $10^\circ$ . Results for pressure (Fig. 4.12) and heat transfer (Fig. 4.13) distribution show a qualitative increase as wedge angle increases. Note, however, that the calculated pressure aft of the nose is higher than either of the two limits. This phenomena is produced by molecular collisions that take place in the flowfield near the wall. These collisions (not modeled in either limit) have the effect of boosting the pressure and heat transfer to appreciable non-zero values.

### 4.3 Comparison of 2-D and Axisymmetric Results

The differences between surface and shock-layer properties for hypersonic flow about geometrically similar blunted cones and wedges are well known for continuum flows [80]. This section will examine the

differences observed in the calculated surface quantities for  $5^\circ$  blunted cones and wedges in hypersonic transitional flow.

#### 4.3.1 Temperature jump and wall slip.

Figures 4.14 and 4.15 present a comparison between the temperature jump for a  $5^\circ$  cone and a  $5^\circ$  wedge as a function of the freestream Knudsen number. Results at the stagnation point (Fig. 4.14) and at  $s/R_N = 4.1$  (Fig. 4.15) show the jump values to be significantly greater



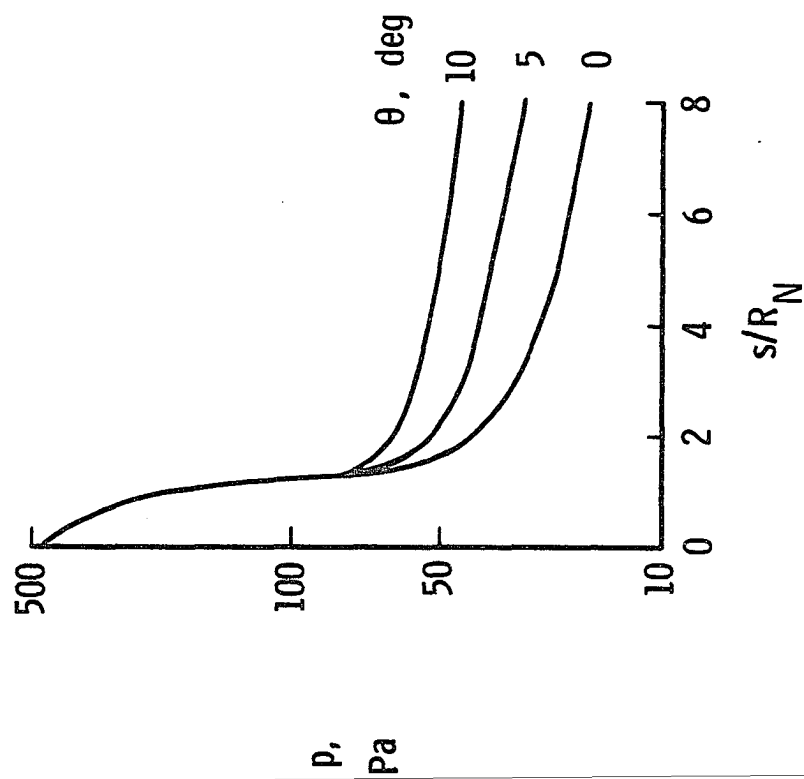


Figure 4.12 Effect of wedge angle on pressure distributions for the 2-D flat plate at 85 km.

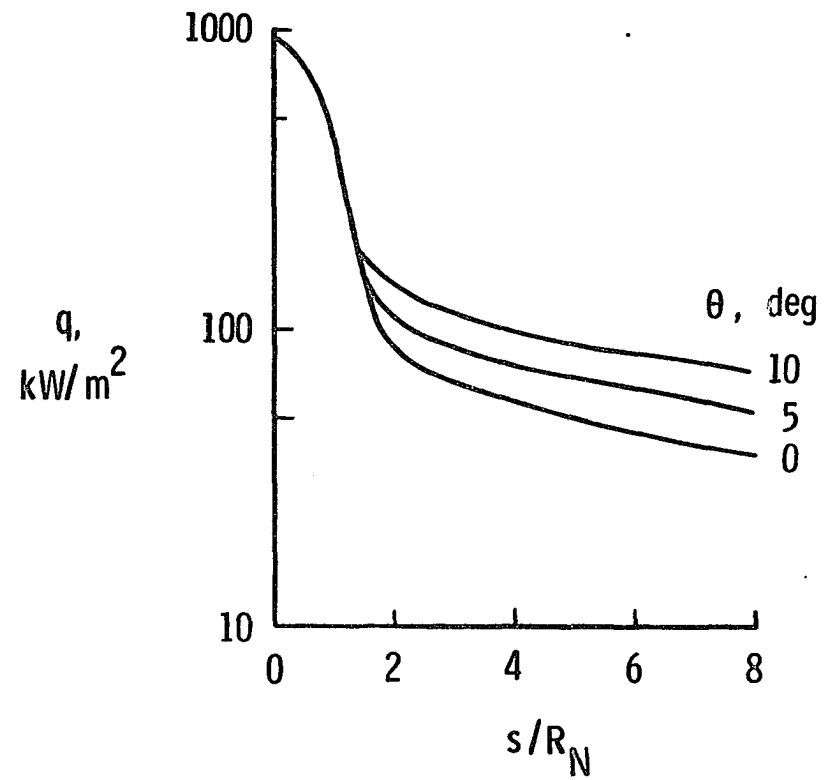


Figure 4.13 Effect of wedge angle on the heat-transfer rate distributions for the 2-D flat plate at 85 km.

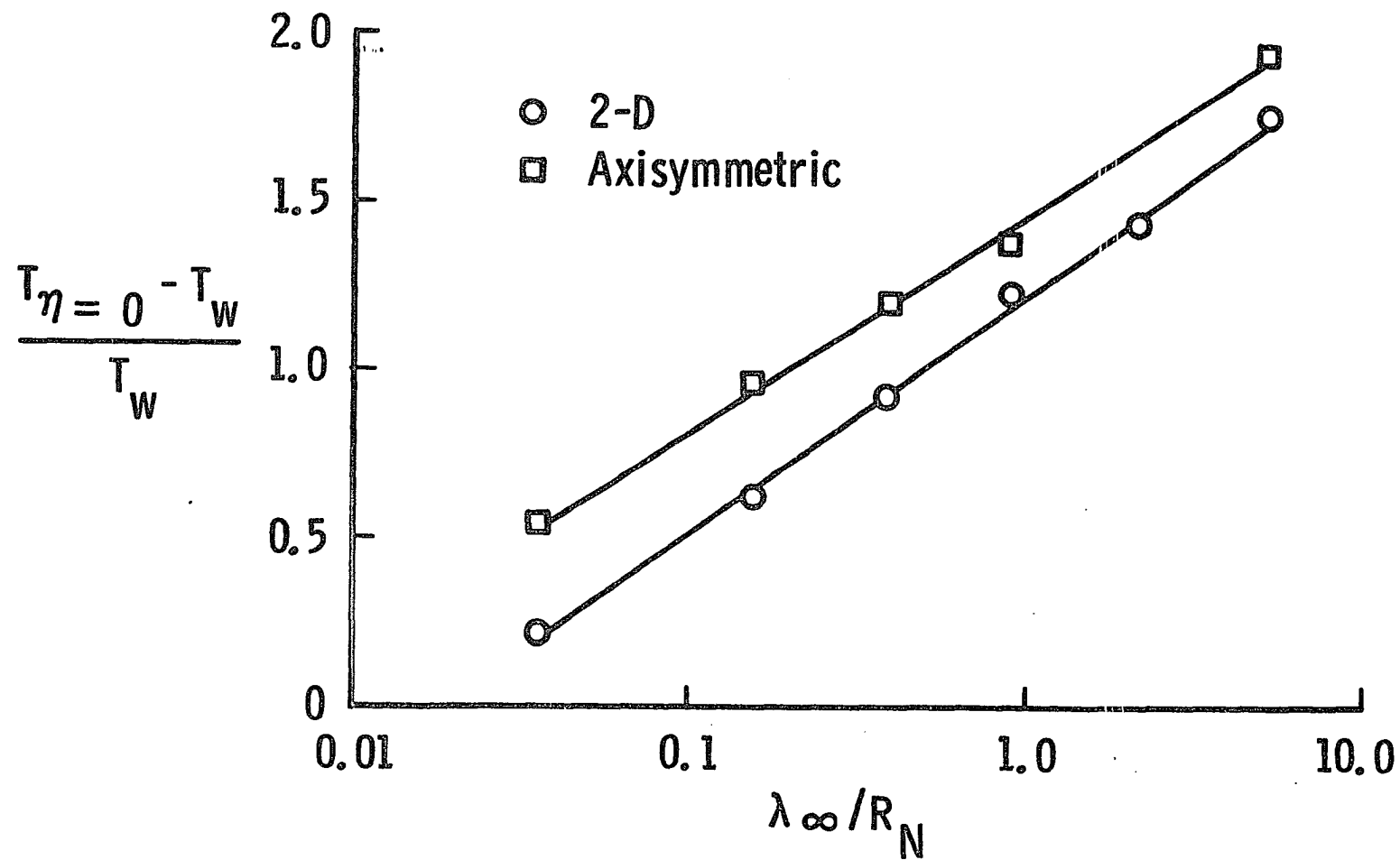


Figure 4.14 Effect of rarefaction on the temperature jump at the stagnation point for the 2-D flat plate at 85 km.

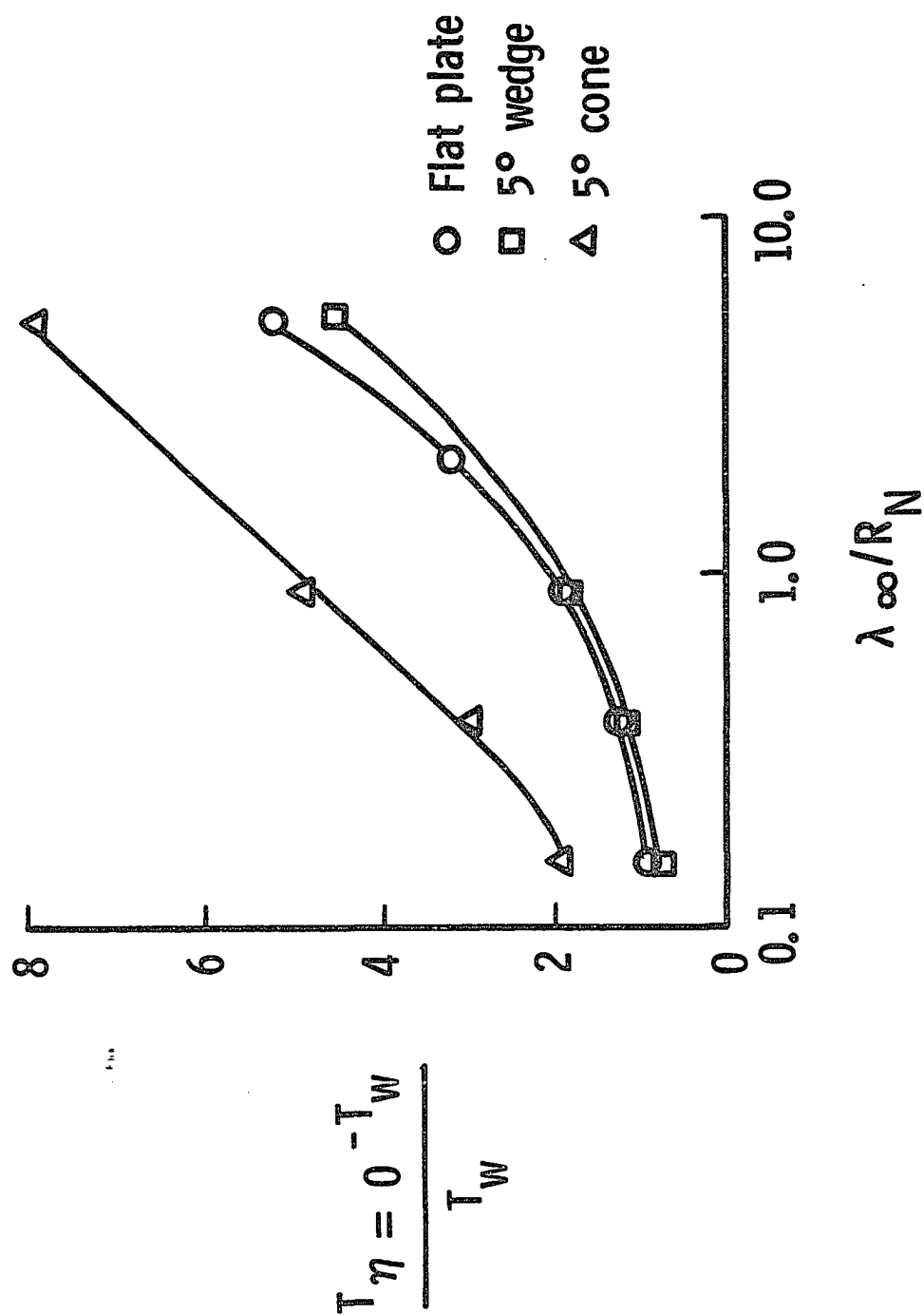


Figure 4.15 Effect of rarefaction on the temperature jump at  $S/R_N = 4.1$  for the 2-D flat plate at 85 km.

for the cone than the geometrically similar wedge or flat plate. The same trend is evident for the velocity slip, as presented in Fig. 4.16, as a function of altitude. This is to be expected since the outer extent of the flowfield disturbance is much smaller for the cone than the corresponding wedge (smaller shock-layer thickness). The cone experiences a more rarefied flow because local gradients are larger than the geometrically similar wedge.

The interrelationship between the body geometry and the degree of rarefaction is clearly demonstrated in Fig. 4.17 where a comparison of the cone and wedge local Knudsen numbers is made along the stagnation streamline for an altitude of 70 km. These results indicate that the local Knudsen number is consistently larger and the shock layer is much thinner for the cone. The flowfield disturbance also differs significantly for the two geometries and will have important implications concerning the gas-phase chemistry and gas-surface catalytic activity. An indication of this effect is presented in Fig. 4.18 where the maximum value of the atomic mass fractions along the stagnation streamline are shown as a function of altitude for both the cone and wedge.

#### 4.3.2 Dissociation.

The onset of dissociation (atomic mass fraction exceeds 1 percent) for oxygen occurs at 96 km for the wedge and at 90 km for the cone. The freestream conditions are free of atomic nitrogen and oxygen and any contribution near the stagnation point is the result of dissociation. Though not apparent from this graph, the 70 km altitude cone has substantial dissociation of diatomic oxygen and this dissociation is complete for the wedge.

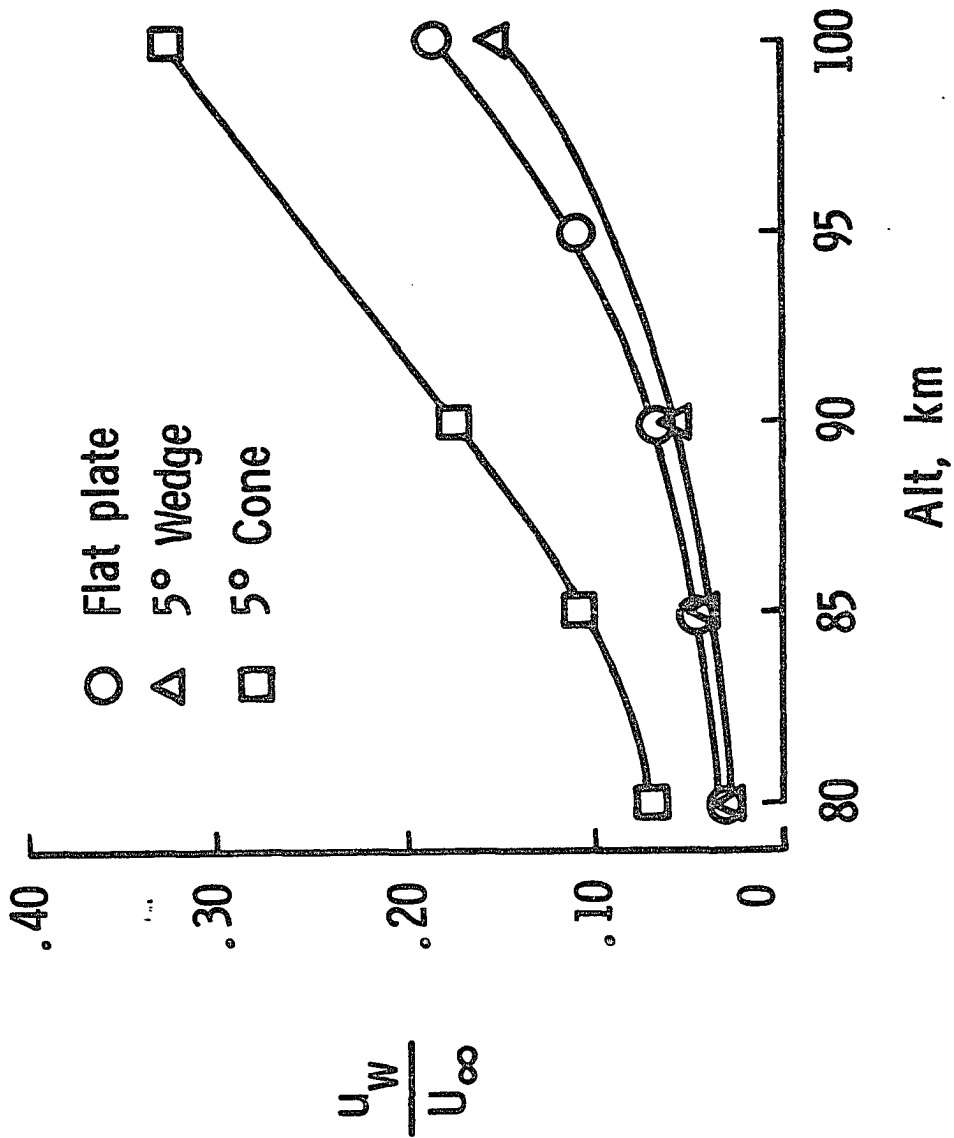


Figure 4.16 Effect of rarefaction on the velocity slip at  $s/R_N = 4.1$ .

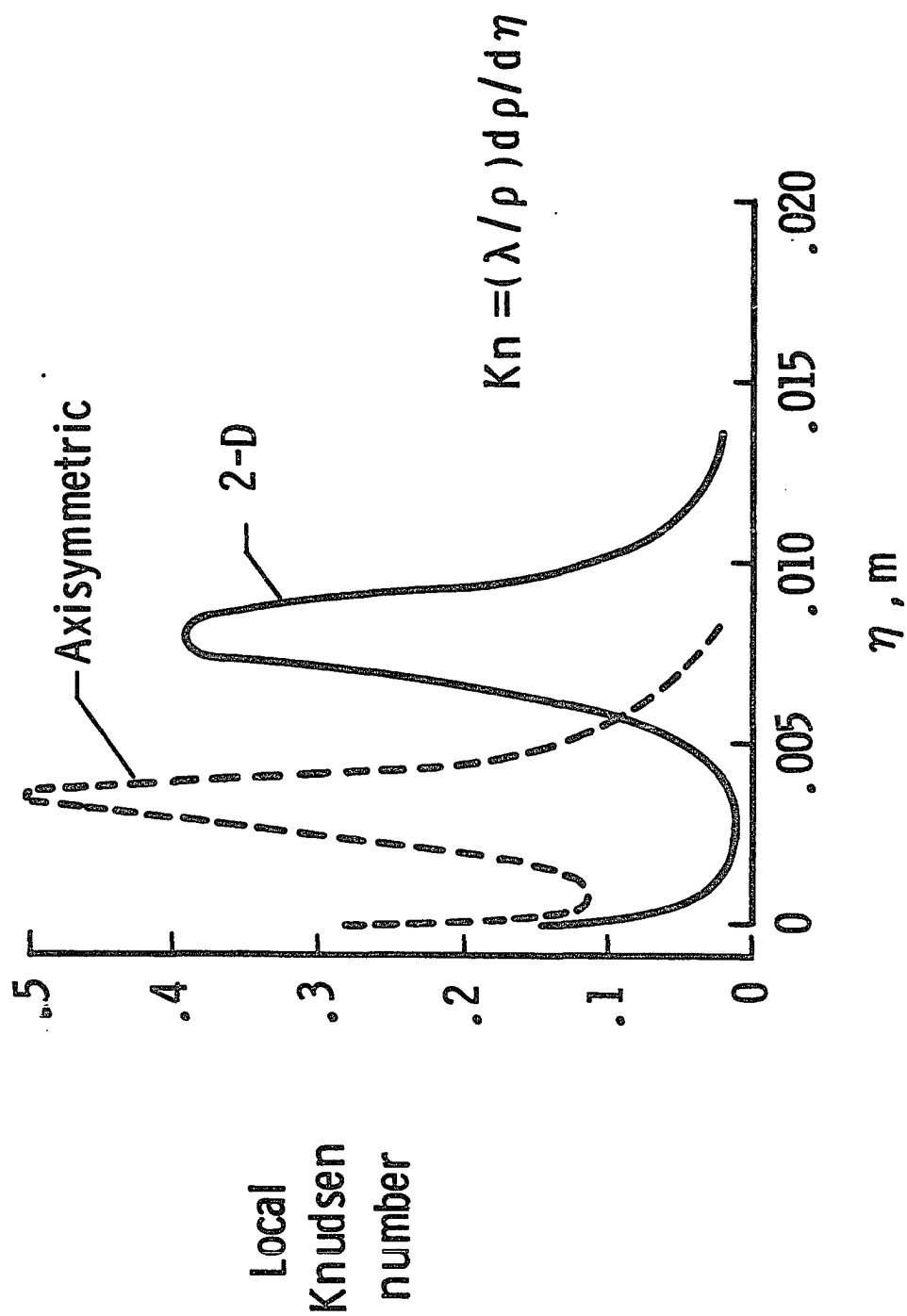


Figure 4.17 Stagnation line Knudsen number variation for the wedge and cone at 70 km.

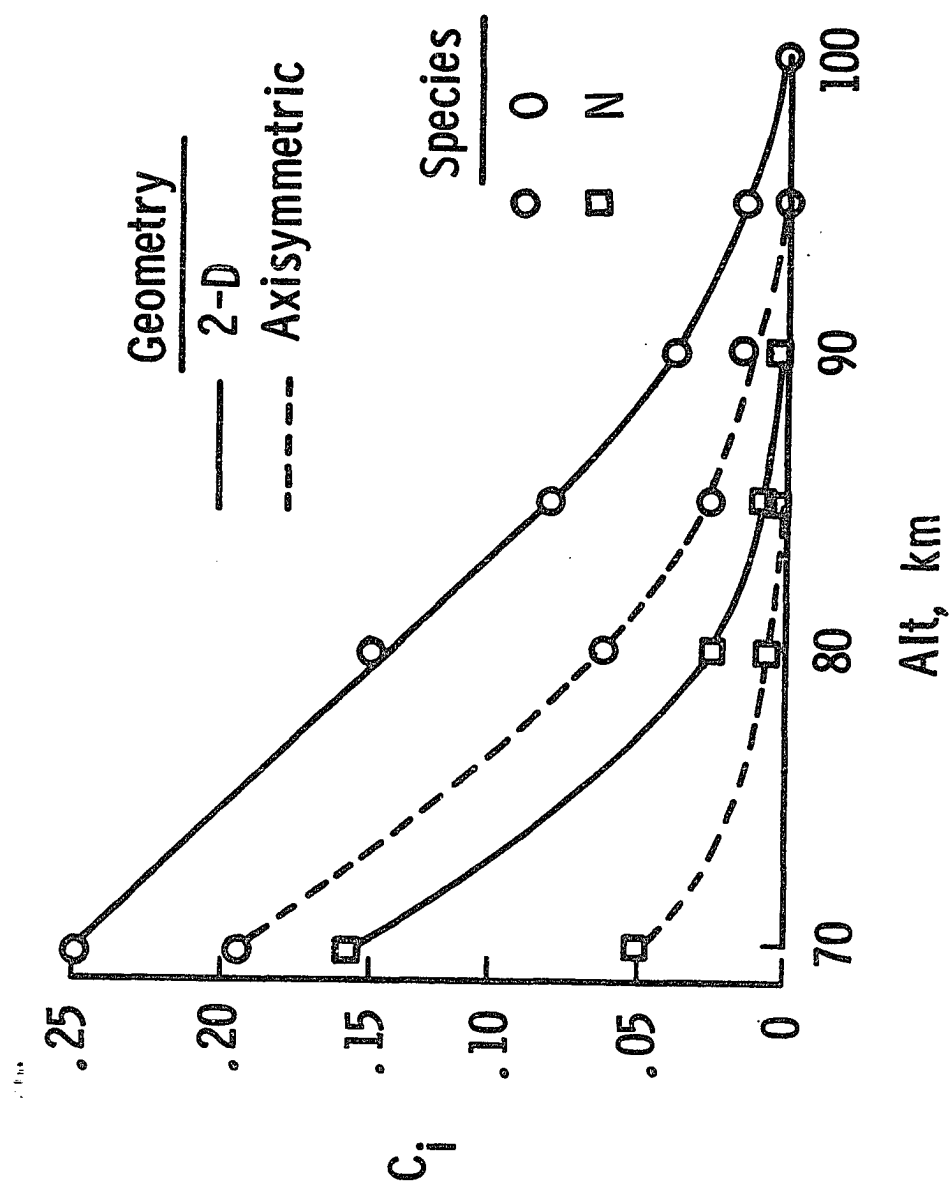


Figure 4.18 Maximum atomic mass fraction values along the stagnation streamline.



#### 4.3.3 Heat-transfer coefficient.

The stagnation point heat-transfer coefficient as a function of freestream Knudsen number is presented in Fig. 4.19 for both the 2-D and axisymmetric bodies. Qualitatively, the results are not surprising. Stagnation heat flux increases from a small value near the continuum regime to a value of unity at the free molecule limit. For the range of freestream conditions considered, the 2-D heat-transfer coefficient is always lower than the corresponding axisymmetric value indicating that less kinetic energy is reaching the surface for the wedge cases.

The stagnation heat flux for the two geometries (see Table 3.4) can be used to indicate further the effects of rarefaction resulting from the flow conditions. In the free molecule limit (see the 100 km case) the ratio of the cone heat flux to wedge heat flux is 1.12 indicating that nearly the same amount of kinetic energy is reaching the surface. The effects of geometry become less important as flow approaches the collisionless flow limit. At 70 km the ratio is 2.79 and shows that geometry is important in the transitional to near continuum limits.

#### 4.3.4 Drag coefficient

The drag coefficient for the plate, 5° wedge and 5° cone, as a function of the freestream Knudsen number, is shown in Fig. 4.20. As with the heat-transfer coefficient, the drag coefficient increases with increasing rarefaction. The change in drag is due primarily to the increase in skin friction rather than a change in pressure coefficient. The difference between the drag coefficients for the flat plate and 5° wedge results from a difference in base area; the drag force for the 5° wedge is only 10 percent greater than that for the plate.

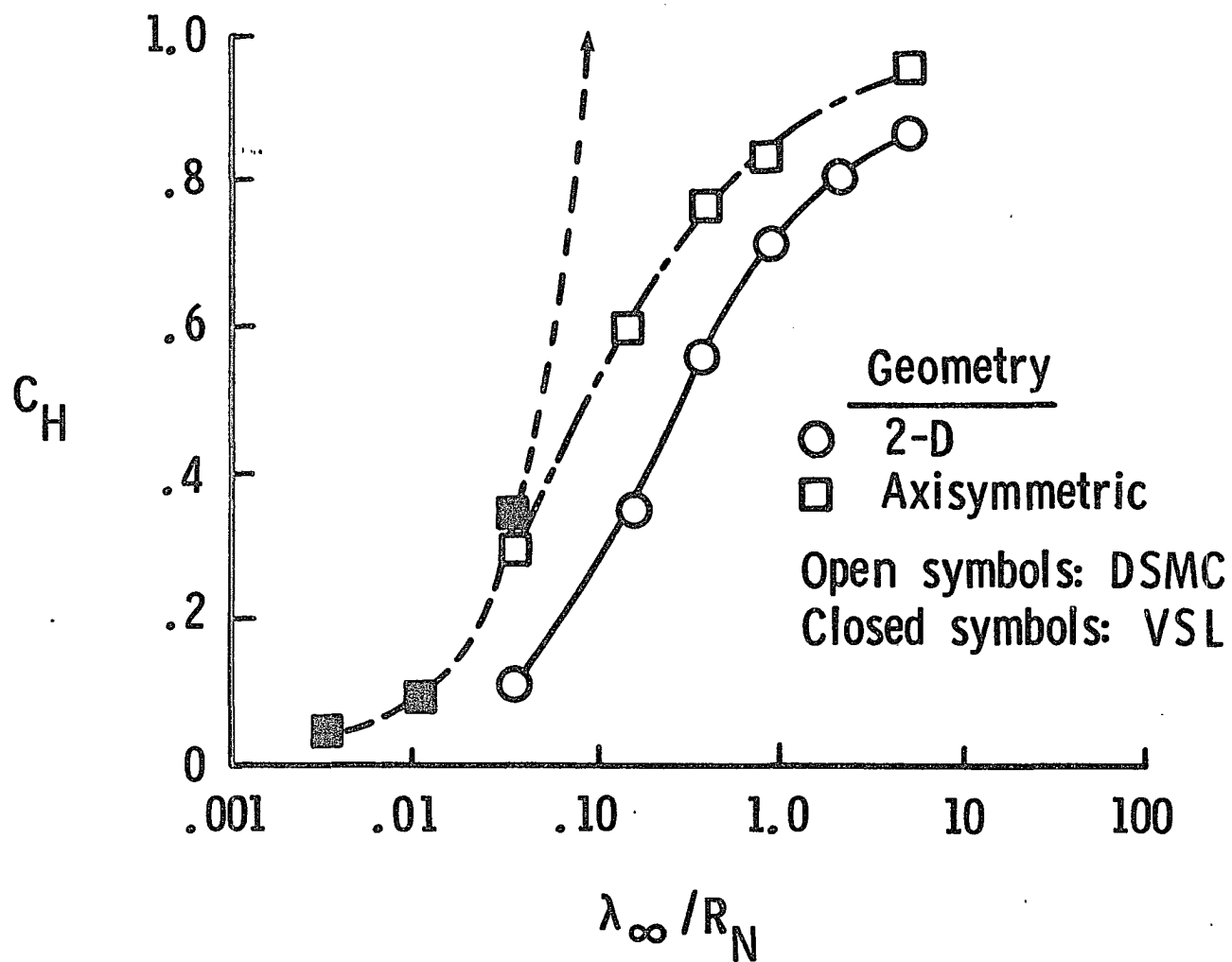


Figure 4.19 Stagnation point heat-transfer coefficient versus freestream Knudsen number.

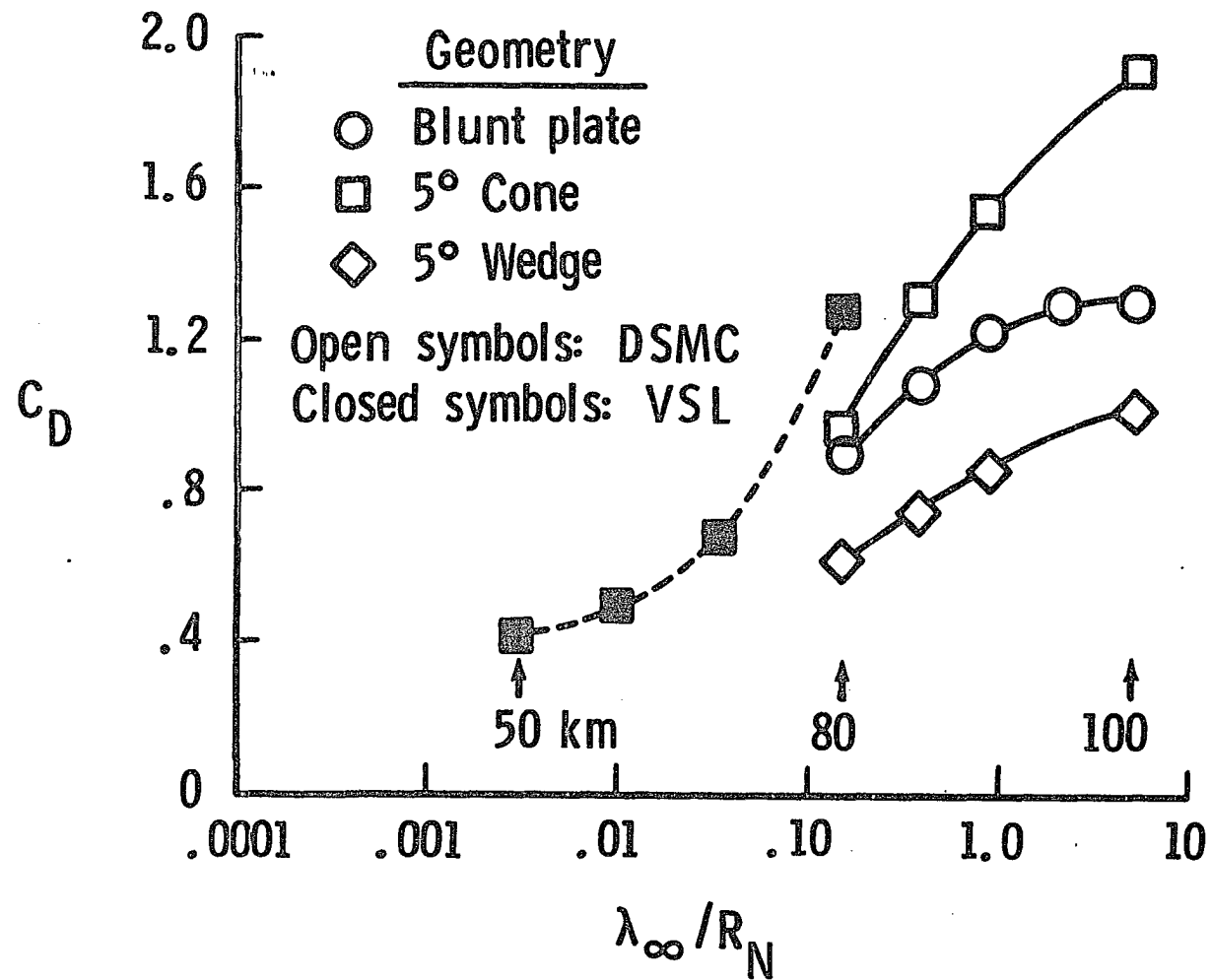


Figure 4.20 Drag coefficient versus freestream Knudsen number.

#### 4.4 Comparison of DSMC and VSL Calculations

The continuum viscous shock layer calculations were made for the 5° cone using the no-slip boundary conditions. Calculations at altitudes of 50, 60, 70 and 80 km were made with the overlap between the VSL and DSMC calculations occurring for the 70 and 80 km cases. However, the only comparisons at 70 km are shown for the stagnation heat transfer rate.

##### 4.4.1 Stagnation streamline comparisons at 70 km.

Figures 4.19 and 4.20 show the extent of the agreement between the two methods for stagnation point heat transfer and body drag. The continuum results begin to depart significantly from the DSMC data above 70 km, particularly the heat transfer predictions. If slip boundary conditions had been used in the VSL calculations, better agreement would occur at the more rarefied conditions.

The computed stagnation point heat-transfer rates differ by 15 percent at 70 km, and there are significant differences between the predicted flowfield structure along the stagnation streamline.

Figures 4.21 and 4.22 present a comparison of the density and temperature profiles along the stagnation streamline. The DSMC calculations for density (Fig. 4.21) show that the upstream influence of the body is more than three times that predicted by the VSL calculation. (Note that the data points shown for the DSMC calculation are only a partial set, particularly near the wall.) The differences shown in the density adjacent to the surface can be explained in part by the temperature jump (537 K) calculated with the DSMC method and by the differences in gas composition adjacent to the wall (Fig. 4.23).

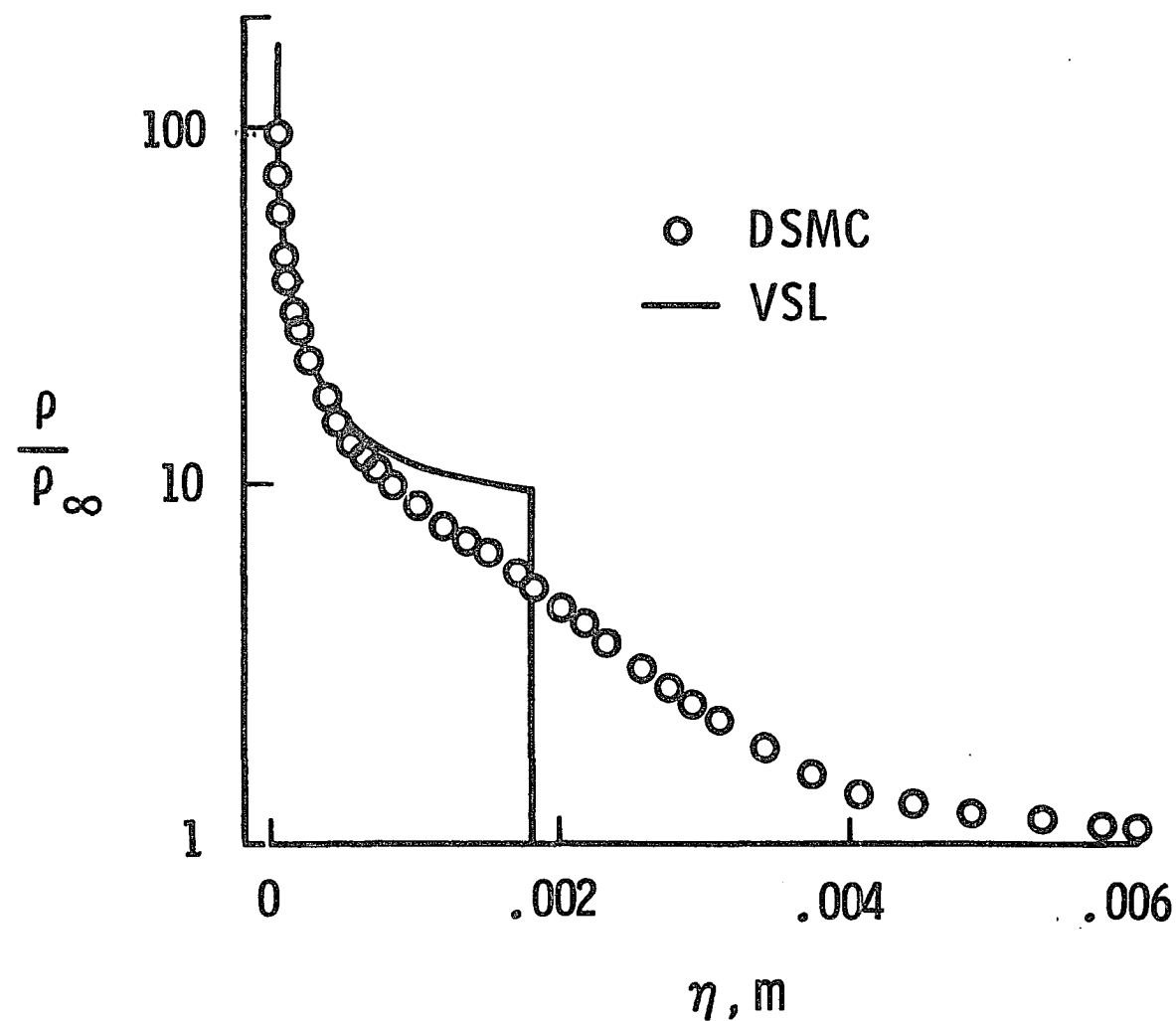


Figure 4.21 Comparison of the calculated stagnation streamline density for the VSL and DSMC 5° cones at 70 km.

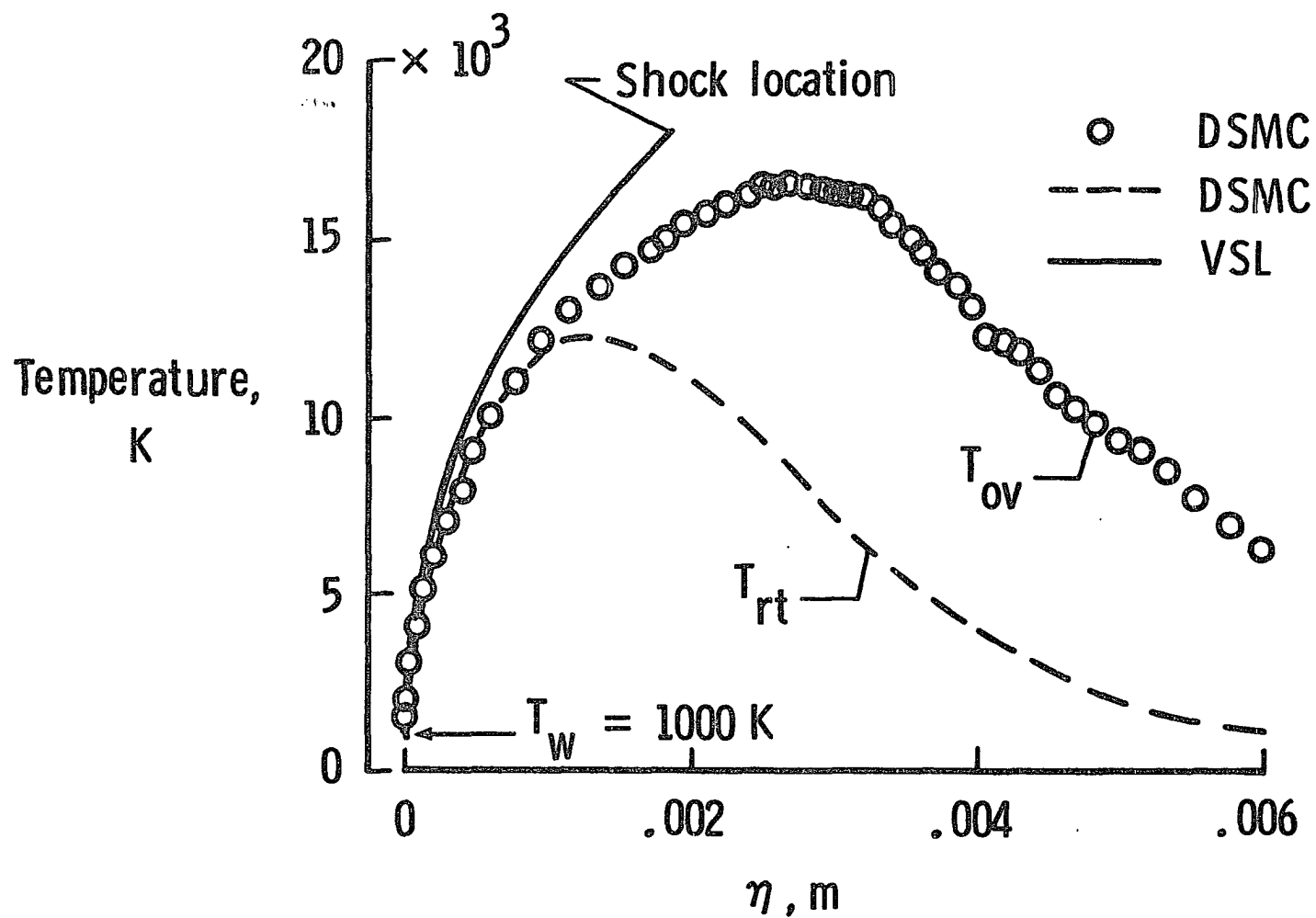


Figure 4.22 Comparison of the stagnation streamline temperature for the VSL and DSMC 5° cone at 70 km.

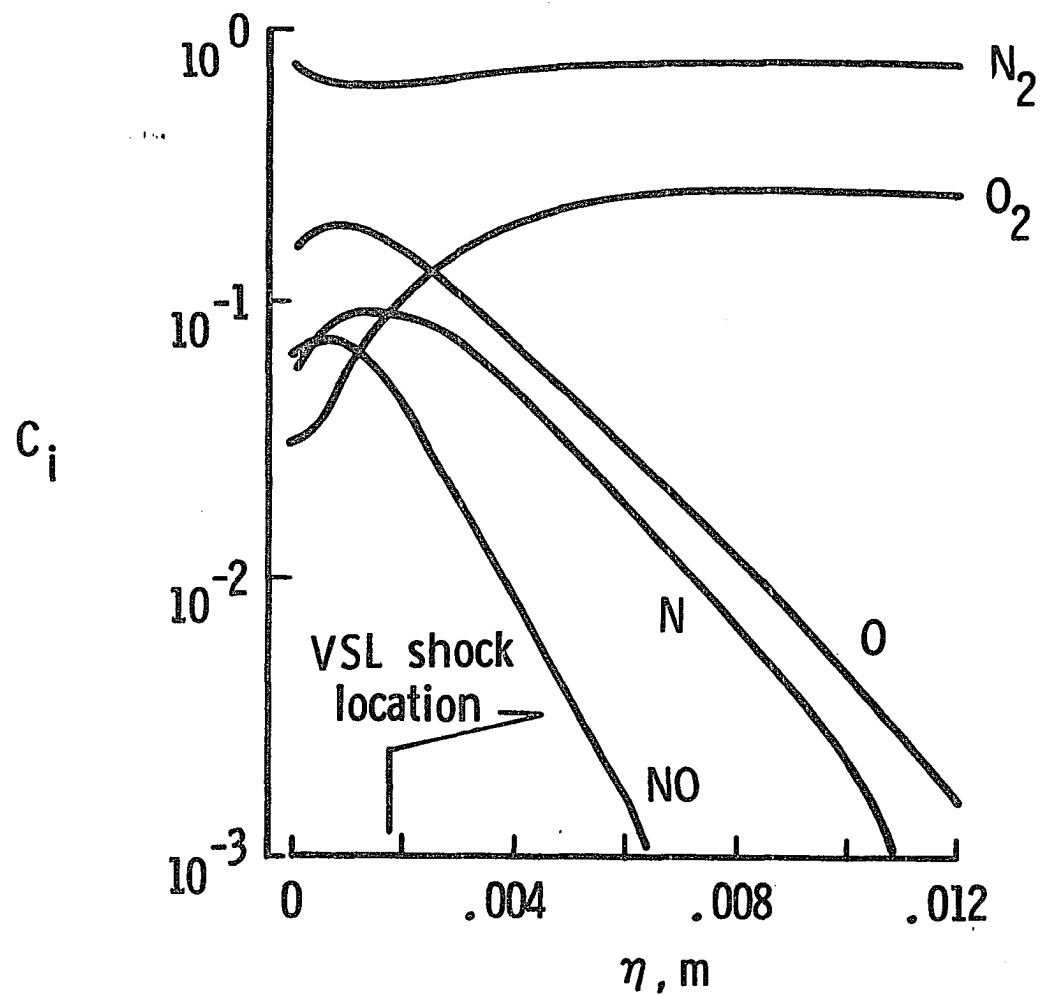


Figure 4.23 Stagnation streamline species mass fraction distributions for the DSMC 5° cone at 70 km.

The stagnation temperature comparison (Fig. 4.22) emphasizes once again the departure of the continuum description in modeling the shock wave structure. As discussed previously, much of the initial overall kinetic temperature rise occurs because of the bimodal velocity distribution producing large velocity separation. The rotational temperature distribution (shown in Fig. 4.22) reflects the effect of collisions which extend many shock-layer thicknesses upstream of the body. Evidence of the effect of the highly energetic collisions within the thick shock wave is presented in Fig. 4.24 where the species mass fraction profiles calculated with the DSMC method are shown. The onset of dissociation is more than six shock-layer thicknesses from the body surface. The large differences in the calculated extent of the flowfield disturbance result in a significant difference in the chemical composition near the surface. This is shown clearly by the atomic oxygen and nitrogen profile comparisons in Fig. 4.24.

#### 4.4.2 Downstream comparisons at 80 km.

The lowest altitude for which an overlap of the downstream DSMC and VSL calculations are made is 70 km. The flow is very rarefied and the VSL calculations should have included slip boundary conditions; however, the comparisons should be instructive concerning the validity of continuum formulations for such problems.

Figure 4.25 presents a comparison of DSMC and VSL density profiles at three locations along the conical flank:  $s/R_N = 2.3, 4.1, \text{ and } 6.3$ . Large differences are obvious in two flow regions: at the wall and at the shock. The wall temperature is specified as 1000 K in both calculations, and the temperature predicted by the DSMC method for the gas adjacent to the wall at the three body stations is 2850, 2942, and



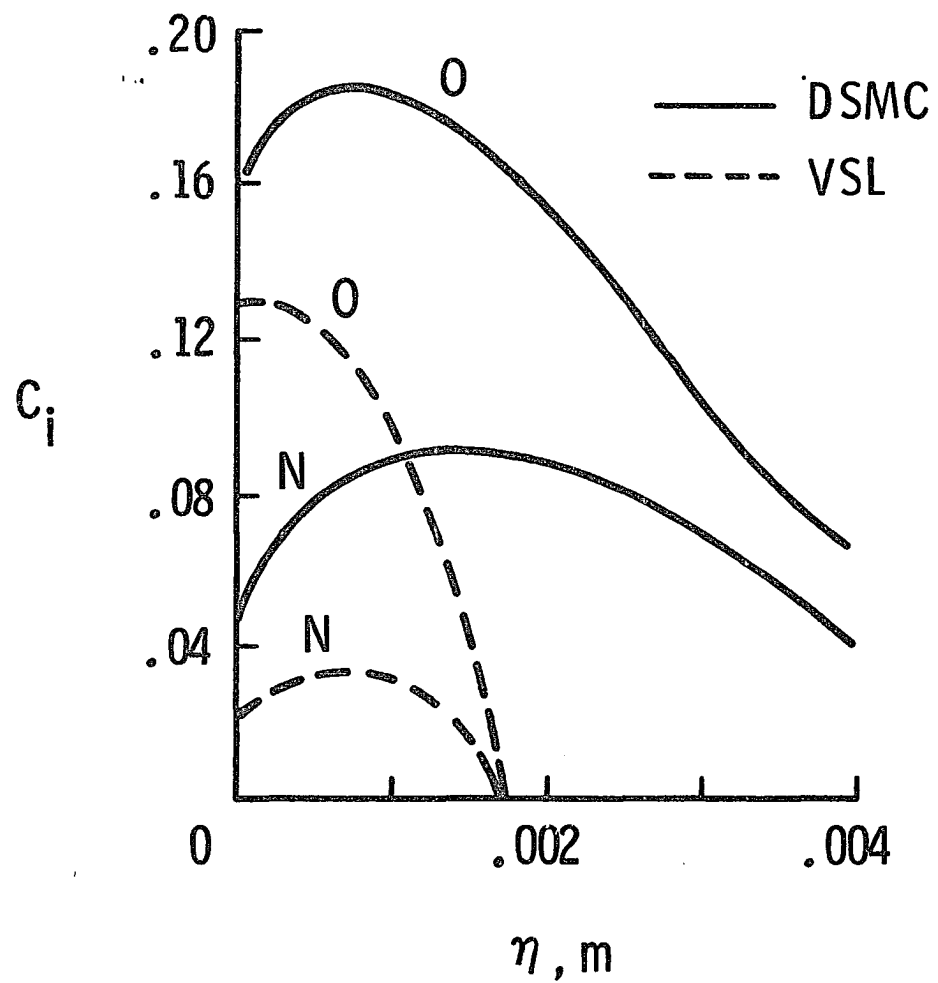


Figure 4.24 Comparison of the stagnation streamline atomic mass fraction distributions for the VSL and DSMC 5° cones at 70 km.

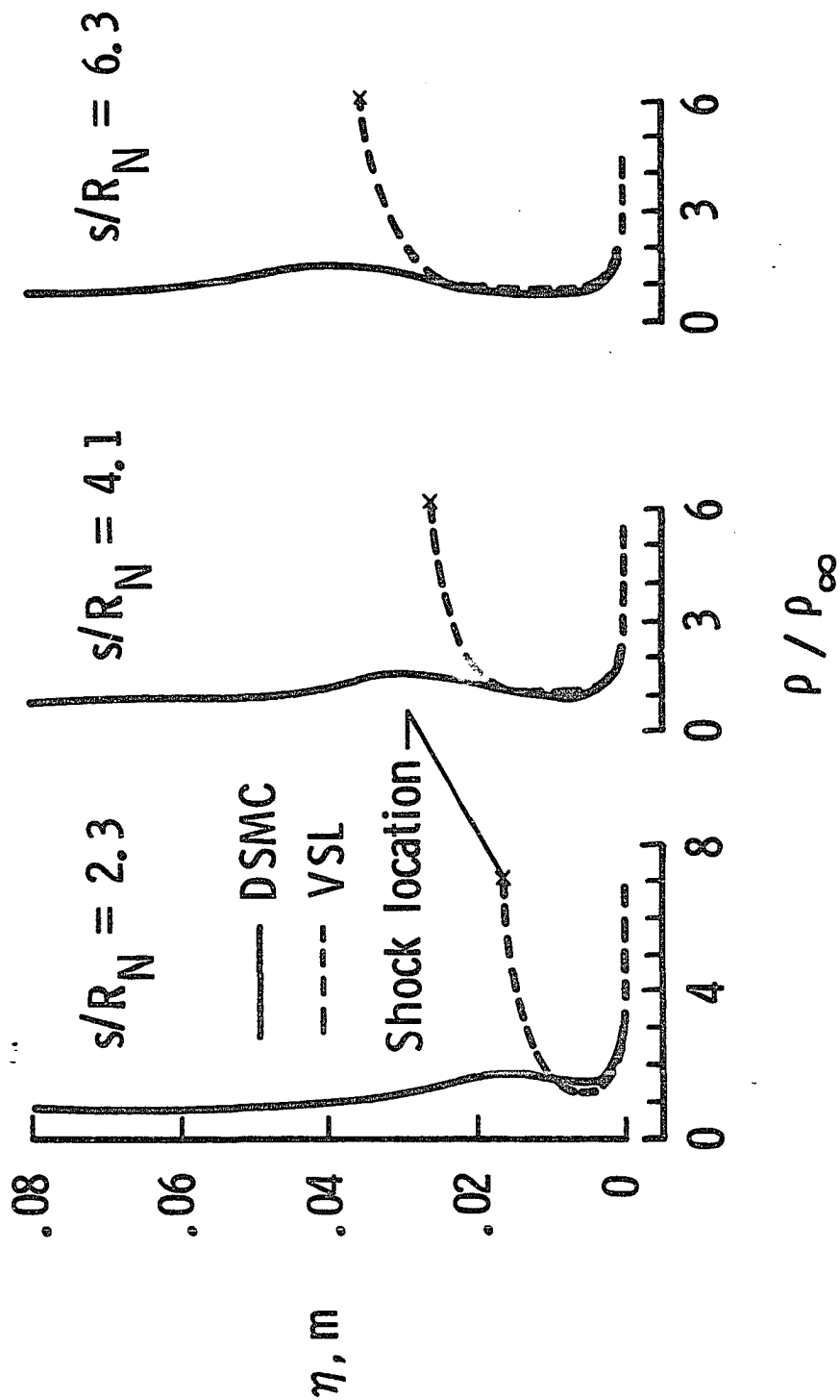


Figure 4.25 Comparison of the calculated density profiles for the VSL and DSMC  $5^{\circ}$  cone at 80 km.

2994 K, respectively. The large temperature jump calculated by the DSMC method produces a much smaller value of wall density.

Major differences in the shock wave structure are observed in the density profile comparisons. Both calculations show that the extent of the flowfield disturbance increases with increasing downstream distance. The outward extent of the flowfield disturbance and the magnitude of the compression within the shock wave differ substantially. The DSMC results show that the shock wave is very thick. The initial density rise occurs over a significant spatial extent as opposed to the discontinuous jump used in the VSL calculations. Maximum  $\rho/\rho_\infty$  values of 1.8 to 1.5 were calculated using DSMC, whereas the VSL predicted corresponding values of 6.9 to 5.8. These results have important implications for possible flight measurements concerning shock layer properties and shock wave location. The differences between the DSMC and VSL calculations are further amplified in Figs. 4.26 and 4.27 where temperature and velocity profile comparisons are presented. For the DSMC calculations, an absence of equilibration between the internal and translational modes exists as the wall is approached (not shown). The same is true of the stagnation results where the differences between the translational and internal kinetic temperatures are small; however, at  $s/R_N = 4.1$ , large differences exist in that the internal kinetic temperature is about one half the translational kinetic temperature. The overall kinetic temperature shown in Fig. 4.26 should not be interpreted as the thermodynamic temperature, which is the quantity shown for the VSL calculation.

In addition to chemical and thermodynamic nonequilibrium, translational nonequilibrium can exist in hypersonic low-density flows

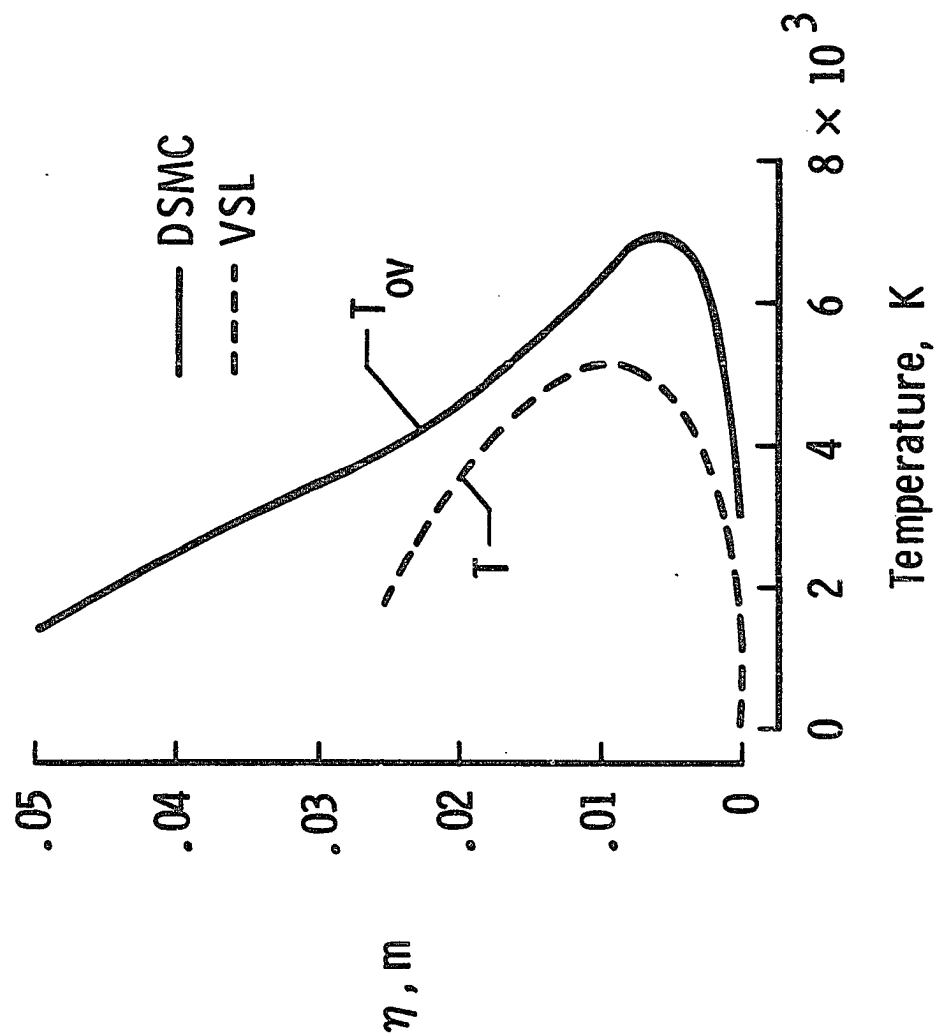


Figure 4.26 Comparison of the overall temperature for the VSL and DSMC 5° cone at 80 km.

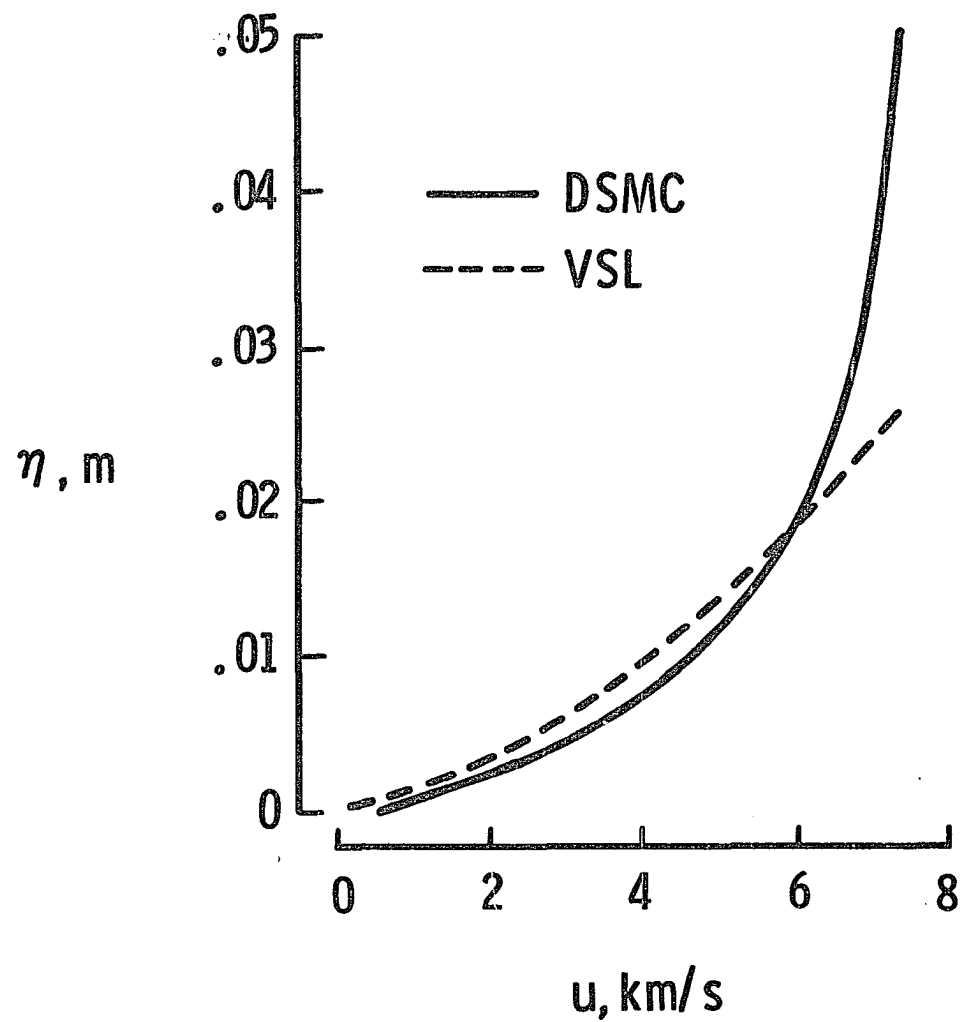


Figure 4.27 Comparison of the tangential velocity for the VSL and DSMC 5° cone at 80 km ( $S/R_N = 4.1$ ).

as is the case for the present calculation. Separate translational kinetic temperatures may be defined for each component direction (see Eq. 1.24, Ref. 31) and the departure of these component temperatures from the translational temperature provides a measure of the translational nonequilibrium in a gas. With translational nonequilibrium, the three normal components of the pressure tensor are not equal and the scalar pressure of a gas is not identical with the normal force per unit area exerted by the gas on a surface. Collectively, the surface "jump" and "slip" values and the shock wave structure are influenced significantly by translational, thermodynamic and chemical nonequilibrium effects. Only by resorting to a particle approach can such effects be modeled realistically in a numerical simulation.

#### 4.5 Comparisons Between Calculations and Experiments

The total temperature corresponding to the freestream conditions used in this study is approximately 28000 K. For low-density hypersonic test facilities, however, the flow energy is much lower than that for the flight conditions considered herein. For example, total temperatures typical of shock tunnels [17,81] are about 6000 K or less, whereas the values for wind tunnels [82-84] are about 4000 K or less. Even so, the energy may be sufficiently high to excite the internal energy modes and produce dissociation.

In an effort to compare the DSMC calculation with measured heat-transfer data, a comparison is made (Fig. 4.28) with the heat-transfer measurements of Boylan [84] for flow about a hemisphere-cylinder with a nose radius of 0.0254 m. Of the test cases reported, the case with a total pressure of 12 atmospheres, a total temperature of 4150 K, a wall

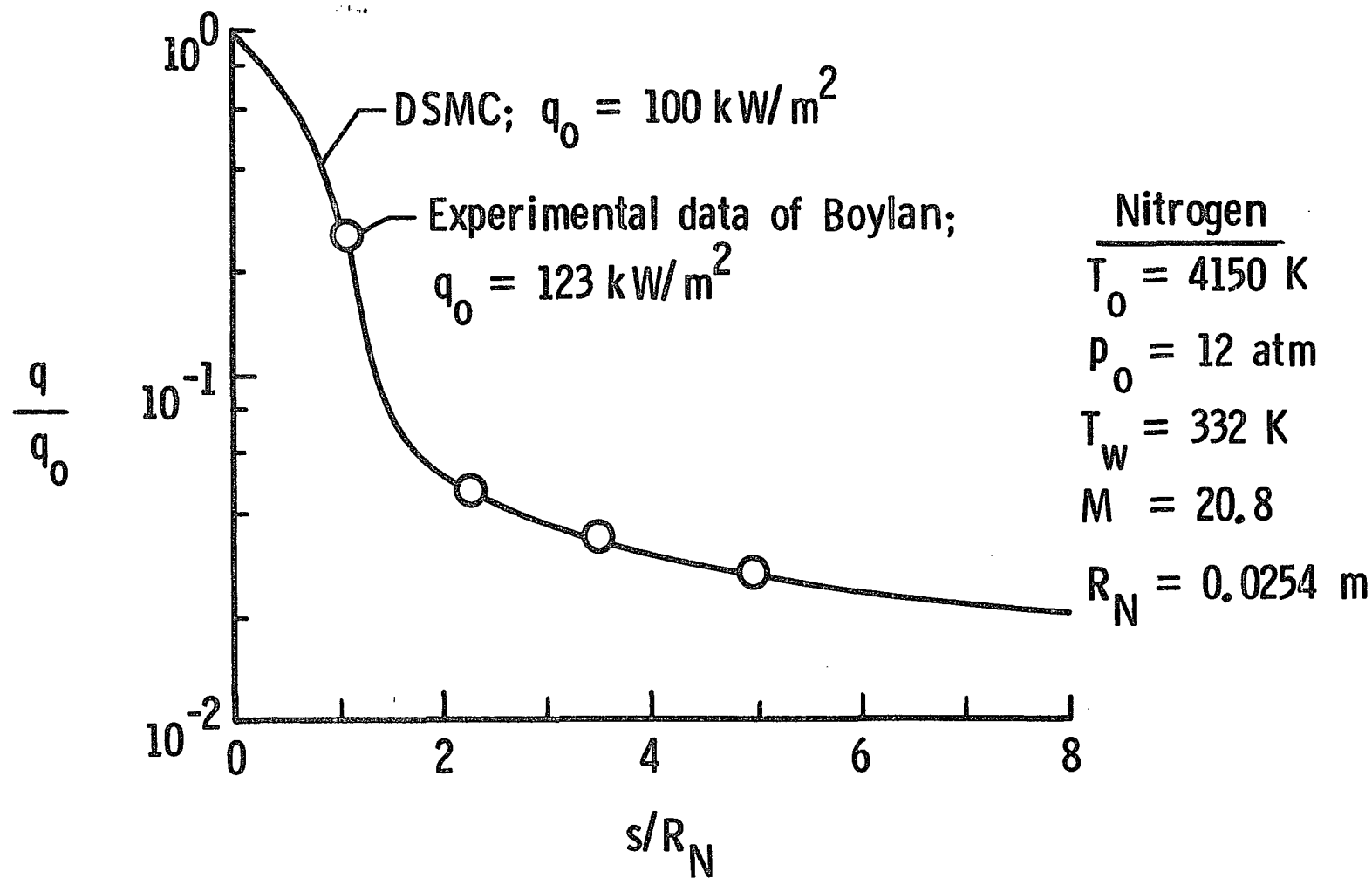


Figure 4.28 Comparison of experimental and DSMC method heat-transfer rate for the spherically blunted cylinder.

temperature of 332 K, and a freestream Mach number of 20.8 was selected for numerical simulation. The test gas was nitrogen.

The freestream conditions used in the numerical simulation are as follows:  $T_\infty = 47.4$  K,  $U_\infty = 2.919$  km/s, and  $\rho_\infty = 1.378 \times 10^{-5}$  kg/m<sup>3</sup> and correspond to a perfect gas isentropic expansion from the stilling chamber while using a value of 1.4 for the ratio of specific heats.

The calculated and measured heat-transfer ratio ( $q/q_0$ ) distributions are in excellent agreement (Fig. 4.28) yet the calculated stagnation point heat-transfer rate is 19 percent lower than the measured value. If the assumption made for the perfect gas isentropic expansion is reconsidered, a difference of approximately 19 percent would be expected. For the stilling chamber conditions, the gas would be in thermal equilibrium and the vibrational energy mode for nitrogen would be 65 percent excited. (See Ref. 41, page 135.) This level of vibrational excitation would produce a value of  $\gamma$  equal to 1.3 and about 21 percent of the energy of the gas would be in the vibrational mode. Since the energy of vibration is not accounted for in the constant  $\gamma = 1.4$  expansion used to define the freestream conditions, it is clear that the heat-transfer rate would be substantially higher than the value calculated.\* To perform a numerical simulation accurately, the freestream state of the gas has to be known so that the thermal state of the gas can be modeled properly as it is introduced into the computational domain. In the current simulation, the molecules are introduced at the outer (freestream) computational boundary at an equilibrium condition corresponding to the freestream temperature of 47.4 K, thereby neglecting any vibrational energy input.



At some point in the expansion from the stilling chamber, the vibrational energy becomes frozen and the low-density shock-layer is essentially transparent to the frozen vibrational energy. Consequently, the transport of energy to the surface is enhanced since the vibrational energy is fully recovered at the surface if full thermal accommodation occurs. It should also be noted that the comparisons Boylan [84] made with the VSL stagnation-point heating predictions using slip boundary conditions show the calculations to be on the low side of the experimental data; probably for the same reason that the current DSMC calculations are low with respect to the measured values.

---

\*Note that the  $\gamma$  of 1.4 is actually an artificial  $\gamma$  used to define the expansion process. Without resorting to a detailed nonequilibrium expansion calculation, the use of the artificial  $\gamma$  is appropriate since the energy modes contributing to the expansion are primarily rotation and translation.

## Chapter 5

### CONCLUSIONS

Particle approaches to hypersonic flows evolved from the need to simulate the molecular motion and collision frequency of the transitional flow regime. The uncoupling of the motion and collision processes has permitted the study of flows that are not amenable to continuum analysis. Numerical simulations are applicable where experimental work is either impractical or impossible. The particle approach is computationally demanding in terms of resources, but it does provide a means of simulating the physics of real gas flows.

The numerical results presented here focused on the nonequilibrium aspects of hypersonic flows in the transitional regime. Comparisons of data calculated with particle and continuum methods has delineated the range of validity for the continuum methods. The DSMC method was used to study the flowfield structure and surface quantities about blunt bodies during nominal reentry conditions. Results of the calculations showed that for the two-dimensional cases, the continuous shock wave structure associated with continuum flow existed along the stagnation streamline at low altitudes, but as rarefaction altitude increased, a gradual merging of the shock layer and shock wave took place. Translational, thermodynamic and chemical nonequilibrium occurred throughout most of the flowfield influenced by the body, as evidenced by the

multiple temperature description of the gas and by the position dependent specie concentration throughout the flow. These results showed the need to address numerical studies of a rarefied gas at the fundamental property level (specie number density, collision frequency and velocity) because these descriptions do not require a priori knowledge of the nonequilibrium nature of the flow.

Comparisons for geometrically similar wedges and cones at identical freestream conditions and Knudsen numbers showed a substantial difference in the degree of rarefaction between the two configurations. The cone experienced a more rarefied flow than the geometrically similar wedge and the onset of significant dissociation occurred at 96 km for wedge flows and 90 km for cone flows. Calculated surface temperature jump and velocity slip were significant for the conditions investigated with larger jump and slip conditions at the aft end of the body than for the nose region.

Comparisons of the particle approach to the viscous shock-layer calculations indicated a large difference in flow structure and surface quantities between the two methods. The DSMC method predicted a larger flowfield disturbance and greater flowfield chemistry and surface recombination.

Good agreement between the DSMC and wind tunnel heat transfer data for moderately energetic flows at low-density hypersonic conditions provided improved confidence in the numerical calculations for simulated reentry conditions, but appropriate experimental data were not available. This study highlighted some of the difficulties encountered in making comparisons with experimental data and the necessity of having detailed information concerning the freestream conditions when dealing

with a nonperfect gas. Also, the results of the comparison showed that the calculated and measured nondimensional heat-transfer distributions were in excellent agreement. Furthermore, the magnitude of the heating rates would have been in good agreement if the actual freestream conditions had been modeled more completely for the numerical simulation. The ability of the DSMC method to predict the features of the flow in the stagnation and highly expanded downstream regions for moderately energetic flows, has been demonstrated. This work should provide increased confidence in applying Direct Simulation Monte Carlo methods to the more energetic flows which are likely to occur around advanced hypersonic vehicles.

## REFERENCES

1. Anderson, J. D. "A Survey of Modern Research in Hypersonic Aerodynamics," AIAA 17th Fluid Dynamics, Plasma Dynamics, and Lasers Conference, Snowmass, Colorado, June 25-27, 1984, AIAA Paper 84-1578.
2. Baker, R. M. L., Jr., and Charwat, A. F., "Transitional Correction to the Drag of a Sphere in Free Molecule Flow," Physics of Fluids, Vol. 1, 1958, pp. 73-81.
3. Oguchi, H., "The Sharp Leading Edge Problem in Hypersonic Flow," in Rarefied Gas Dynamics, ed. L. Talbot, Academic Press, New York, 1961, pp. 501-524.
4. Ho, H. and Probstein, R. F., "The Compressible Viscous Layer in Rarefied Hypersonic Flow," in Rarefied Gas Dynamics, ed. L. Talbot, Academic Press, New York, 1961, pp. 525-552.
5. Grad, H., "Asymptotic Theory of the Boltzmann Equation, II," in Rarefied Gas Dynamics, ed. J. A. Laurmann, Academic Press, New York, 1963, pp. 26-59.
6. Janos, W. A., "On the Convergence and Error Estimation of the Iterative Solution of the Nonlinear Boltzmann Equation," in Rarefied Gas Dynamics, ed. J. A. Laurmann, Academic Press, New York, 1963, pp. 60-74.
7. Eldred, C. H., "Shuttle II - The Next Generation," AIAA 24th Aerospace Sciences Meeting, Reno, Nevada, January 6-9, 1986, AIAA Paper 86-0191.
8. Potter, J. L., "The Transitional Rarefied-Flow Regime," in Rarefied Gas Dynamics, C. L. Brundin ed., Academic Press, New York, 1967, pp. 881-937.
9. Sherman, F. S., "The Transition From Continuum to Molecular Flow," Annual Review of Fluid Mechanics, Vol. 1, 1969, ed. by W. R. Sears and M. Van Dyke, pp. 317-340.
10. Probstein, R. F., "Continuum Theory and Rarefied Hypersonic Aerodynamics," in Rarefied Gas Dynamics, F. M. Devienne ed., 1960, pp. 416-431.
11. Probstein, R. F., "Aerodynamics of Rarefied Gases," in Rarefied Gas Dynamics, F. M. Devienne ed., 1960, pp. 258-275.

12. Street, R. E., "A Study of Boundary Conditions in Slip-Flow Aerodynamics," in Rarefied Gas Dynamics, F. M. Devienne ed., Pergamon Press, 1960, pp. 276-292.
13. Gupta, R. N. and Simmons, A. L., "Hypersonic Low-Density Solutions of the Navier-Stokes Equations with Chemical Nonequilibrium and Multicomponent Surface Slip," AIAA/ASME 4th Joint Thermophysics and Heat Transfer Conference, Boston, Massachusetts, June 2-4, 1986, AIAA Paper 86-1349.
14. Allegre, J., Raffin, M. and Gottesdiener, L., "Slip Effects on Supersonic Flowfields Around NACA 0012 Airfoils, 15th Symposium on Rarefied Gas Dynamics, Grado, Italy, June 16-20, 1986.
15. Howe, J. T. "Introductory Aerothermodynamics of Advanced Space Transportation Systems," January 1983, AIAA Paper 83-0406.
16. Rao, S. R., Surface Phenomena, Chapter 8, 1972.
17. Vidal, R. J., "High Temperature Phenomena in Hypersonic Flows-Final Report," AEDC-TDR-64-143, June 1964.
18. Anderson, L. A., "Effect of Surface Catalytic Activity on Stagnation Heat-Transfer Rates," AIAA Journal, Vol. 11, May 1973, pp. 649-656.
19. Scott, C. D., "Catalytic Recombination of Nitrogen and Oxygen on High Temperature Reusable Surface Insulation," in Progress in Astronautics and Aeronautics, Vol. 77, 1981, pp. 192-212.
20. Neuenschwander, W. E., McBride, D. U. and Armour, G. A., "Shuttle TPS Thermal Performance and Analysis Methodology," in NASA Conference Publication 2283, Shuttle Performance: Lessons Learned, compiled by J. P. Arrington and J. J. Jones, 1983, pp. 1025-1064.
21. Moss, J. N. and Bird, G. A., "Direct Simulation of Transitional Flow for Hypersonic Reentry Conditions," Progress in Astronautics and Aeronautics; Thermal Design of Aeroassisted Orbital Transfer Vehicles, ed. H. F. Nelson, Vol. 96, 1985, pp. 113-139.
22. Riesco-Chueca, P., Fernandez-Feria, R. and de la Mora, J. F., "Nonlinearities in the Interspecies Transfer of Momentum and Energy for Disparate-Mass Gas Mixtures and Shock Wave Structure," 15th Symposium on Rarefied Gas Dynamics, Grado, Italy, June 16-20, 1986.
23. Meolans, J. G. and Brun, R., "Nonequilibrium Vibrational Population Behind Shock Waves: Comparison Theory - Experiments," the 15th Symposium on Rarefied Gas Dynamics, Grado, Italy, June 16-20, 1986.
24. Chung, P. M., Holt, J. F. and Liu, S. W., "Merged Stagnation Shock Layer of Nonequilibrium Dissociating Gas," AIAA Journal, Vol. 6, December 1968, pp. 2372-2379.

25. Park, C., "Problems of Rate Chemistry in the Flight Regimes of Aeroassisted Orbital Transfer Vehicles," AIAA 19th Thermophysics Conference, Snowmass, Colorado, June 25-28, 1984, AIAA Paper 84-1730.
26. Robben, F. and Talbot, L., "Measurements of Rotational Temperatures in a Low-Density Wind Tunnel," Physics of Fluids, Vol. 9, April 1966, pp. 644-652.
27. Bird, G. A., "Breakdown of Translational and Rotational Equilibrium in Gaseous Expansions," AIAA Journal, Vol. 8, November 1970, pp. 1998-2003.
28. Bird, G. A., "Direct Simulation of the Incompressible Kramers Problem," in Progress in Astronautics and Aeronautics, Vol. 51, 1977, L. Potter ed., pp. 323-333.
29. Reynolds, M. A., Smolderen, J. J. and Wendt, J. F., "Velocity Profile Measurements in the Knudsen Layer for the Kramers Problem," Rarefied Gas Dynamics, G. Koppenwallner ed., 1974, pp. A.21-1 to A.21-14.
30. Willis, D. R., "Comparison of Kinetic Theory Analysis of Linearized Couette Flow," Physics of Fluids, Vol. 5, February 1962, pp. 127-135.
31. Bird, G. A., Molecular Gas Dynamics, Clarendon Press, Oxford, 1976.
32. Bird, G. A., "Monte Carlo Simulation of Gas Flows," Annual Reviews of Fluid Mechanics, Vol. 10, ed. M. D. Van Dyke et al., Annual Reviews Inc., Palo Alto, 1979, p. 11.
33. Tien, C. L. and Lienhard, J. H., Statistical Thermodynamics, Hemisphere Publishing Corporation, 1979, pp. 29, 305.
34. Hirschfelder, J. O., Curtiss, C. F. and Bird, R. B., Molecular Theory of Gases and Liquids, John Wiley and Sons, New York, 1964, pp. 31-35.
35. Macrossan, M. N., "Diatomic Collision Models Used in the Monte-Carlo Direct Simulation Method Applied to Rarefied Hypersonic Flows," Doctoral Thesis, Imperial College, University of London, September 1983.
36. Lennard-Jones, J. E. and Devonshire, A. F., "Critical and Co-operative Phenomena III. A Theory of Melting and the Structure of Liquids," Proceedings of the Royal Society, Series A1, Vol. 169, December 1938, pp. 317-338.
37. Buckingham, R. A. and Corner, J., "Tables of Second Virial and Low-Pressure Joule-Thomson Coefficients for Intermolecular Potentials with Exponential Repulsion," Proceedings of the Royal Society, Series A, Vol. 189, March 1947, pp. 118-129.

38. Corner, J., "The Second Virial Coefficient of a Gas of Non-Spherical Molecules," Proceedings of the Royal Society, Series A, Vol. 192, February 1948, pp. 275-292.
39. Rice, W. E. and Hirschfelder, J. O., "Second Virial Coefficients of Gases Obeying a Modified Buckingham (Exp-Six) Potential," Journal of Chemical Physics, Vol. 22, February 1954, pp. 187-192.
40. Bird, G. A., "Definition of Mean Free Path for Real Gases," Physics Fluids, Vol. 26, November 1983, pp. 3222-3223.
41. Vincenti, W. G. and Kruger, C. H., Introduction to Physical Gas Dynamics, Krieger Publishing Company, 1982.
42. Epstein, R. and Craxton, R. S., "Statistical Ray Tracing in Plasmas with Random Density Fluctuations," Physical Review A, Vol. 33, March 1986, pp. 1892-1902.
43. Hornstein, J. and Fainberg, J., "Ray Methods in Random Media," Proceedings of SPIE - The International Society for Optical Engineering, Washington, D.C., R. W. Fenn, ed., April 21-22, 1981.
44. Clark, M. Jr., and Hansen, K. F., Numerical Methods of Reactor Analysis, Academic Press, New York, 1964, pp. 239-277.
45. Davis, D. H., "Monte Carlo Calculation of Molecular Flow Rates Through a Cylindrical Elbow and Pipes of other Shapes," Journal of Applied Physics, Vol. 31, July 1960, pp. 1169-1176.
46. Alder, B. J. and Wainwright, T., "Molecular Dynamics by Electronic Computers," in Transport Processes in Statistical Mechanics, ed. I. Prigogine, Interscience, New York, 1958, pp. 97-131.
47. Bird, G. A., "Direct Simulation of Gas Flows at the Molecular Level," Presented at the First World Congress on Computational Mechanics, University of Texas at Austin, September 22-26, 1986.
48. Moss, J. N. and Bird, G. A., "Monte Carlo Simulation in Support of the Shuttle Upper Atmosphere Mass Spectrometer Experiment," AIAA 20th Thermophysics Conference, Williamsburg, Virginia, June 19-21, 1985, AIAA Paper 85-0968.
49. Moss, J. N., "Direct Simulation of Hypersonic Transitional Flow," 15th International Symposium on Rarefied Gas Dynamics, Grado, Italy, June 16-20, 1986.
50. Bird, G. A., "Rarefied Hypersonic Flow Past a Slender Shape Cone," in Rarefied Gas Dynamics, O. M. Belotserkovskii et al. ed., 1986, Plenum Press, pp. 349-356.
51. Bird, G. A., "Direct Simulation and the Boltzmann Equation," Physics of Fluids, Vol. 13, November 1970, pp. 2676-2681.



52. Bird, G. A., "Shock-Wave Structure in a Rigid Sphere Gas," in Rarefied Gas Dynamics, J. H. De Leeuw ed., Academic Press, 1965, pp. 216-222.
53. Bird, G. A., "Direct Molecular Simulation of a Dissociating Diatomic Gas," Journal of Computational Physics, Vol. 25, December 1977, pp. 353-365.
54. Bird, G. A., "Simulation of Multi-Dimensional and Chemically Reacting Flows," in Rarefied Gas Dynamics, R. Campargue ed., 1979, pp. 365-388.
55. Bird, G. A., "Aerodynamic Properties of Some Simple Bodies in the Hypersonic Transition Region," AIAA Journal, Vol. 4, January 1966, pp. 55-60.
56. Harvey, J. K., "Direct Simulation Monte Carlo Method and Comparison with Experiment," AIAA 20th Thermophysics Conference, Williamsburg, Virginia, June 19-21, 1985, AIAA Paper 85-0996.
57. Dahlen, G. A., Macrossan, M. N., Brundin, C. L., and Harvey, J. K., "Blunt Cones in Rarefied Hypersonic Flow; Experiments and Monte-Carlo Simulations," in Rarefied Gas Dynamics, H. Ogrichi, ed., 1986, University of Tokyo Press, Tokyo, pp. 229-240.
58. Schmidt, B., "Electron Beam Density Measurements in Shock Waves in Argon," Journal of Fluid Mechanics, Vol. 39, Part 2, 1969, pp. 361-373.
59. Seiler, F., Schmidt, B. and Kuschnerus, N., "Direct Monte-Carlo Simulation Technique Applied to Some Rarefied Gas Dynamics Problems," 15th Symposium on Rarefied Gas Dynamics, Grado, Italy, June 16-20, 1986.
60. Bird, G. A., "Monte-Carlo Simulation in an Engineering Context," 12th International Symposium on Rarefied Gas Dynamics, Charlottesville, VA, July 7-11, 1980, pp. 239-255.
61. Borgnakke, C. and Larsen, P. S., "Statistical Collision Model for Monte Carlo Simulation of Polyatomic Gas Mixture," Journal of Computational Physics, Vol. 18, 1975, pp. 405-420.
62. Robben, F. and Tabbot, L., "Experimental Study of the Rotational Distribution Function of Nitrogen in a Shock Wave," Physics of Fluids, Vol. 9, April 1966, pp. 653-662.
63. Bird, G. A., "Approach to Translational Equilibrium in a Rigid Sphere Gas," Physics of Fluids, Vol. 6, October 1963, pp. 1518-1519.
64. Parker, J. G., "Rotational and Vibrational Relaxation in Diatomic Gases," Physics of Fluids, Vol. 2, July-August, 1959, pp. 449-462.
65. Carnevale, E. H., "Ultrasonic Determination of Rotational Collision Numbers and Vibrational Relaxation Times of Polyatomic Gases at High Temperatures," Journal of Chemical Physics, Vol. 47, October 1967, pp. 2829-2835.

66. Bird, G. A., "Direct Simulation of Typical AOTV Entry Flows," presented at the AIAA/ASME 4th Thermophysics and Heat Transfer Conference, Boston, MA, June 2-4, 1986, AIAA Paper 86-1310.
67. Bortner, M. H., "Suggested Standard Chemical Kinetics for Flow Field Calculations - A Consensus Opinion. AMRAC Proceedings, Vol. 14. Doc. No. 4613-135-X, Inst. Sci. Technology, University of Michigan, April 18-19, 1966, pp. 569-581.
68. Throckmorton, D. A., "Benchmark Determination of Shuttle Orbiter Entry Aerodynamic Heat-Transfer Data," Journal of Spacecraft and Rockets, Vol. 20, May-June, 1983, pp. 219-224.
69. Zoby, E. V., Gupta, R. N., and Simmonds, A. L., "Temperature-Dependent Reaction Rate Expressions for Oxygen," Progress in Astronautics and Aeronautics: Thermal Design of Aeroassisted Orbital Transfer Vehicles, H. F. Nelson ed., Vol. 96, 1985, pp. 445-464.
70. Cubley, S. J. and Mason, E. A., "Atom-Molecule and Molecule-Molecule Potentials and Transport Collision Integrals for High-Temperature Air Space," Physics of Fluids, Vol. 18, No. 9, September 1975, pp. 1109-1111.
71. Jacchia, L. C., "Thermospheric Temperature, Density, and Composition: New Models," Research in Space Science, SAO Special Report No. 375, March 1977.
72. U.S. Standard Atmosphere, 1962.
73. Thompson, R. A., Private Communication, Aerothermodynamics Branch, NASA Langley Research Center, Hampton, Virginia, 1986.
74. Kim, M. D., Swaminathan, S. and Lewis, C. H., "Three-Dimensional Nonequilibrium Viscous Flow Over the Space Shuttle Orbiter with Surface Catalytic Effects," AIAA 18th Thermophysics Conference, Montreal, Canada, June 1-3, 1983, AIAA Paper 83-0487, January 1983.
75. Thompson, R. A., "Three-Dimensional Viscous Shock-Layer Applications for the Space Shuttle Orbiter," AIAA 23rd Aerospace Sciences Meeting, Reno, Nevada, January 14-17, 1985, AIAA Paper 85-0246.
76. Cuda, V. Jr. and Moss, J. N., "Direct Simulation of Hypersonic Flows Over Blunt Wedges," Journal of Thermophysics and Heat Transfer, Vol. 1, No. 2, April 1987, pp. 97-104.
77. Moss, J. N. and Cuda, V. Jr., "Nonequilibrium Effects for Hypersonic Transitional Flows," to appear in the Journal of Thermophysics and Heat Transfer, 1987.
78. Bird, G. A., "Low-Density Aerothermodynamics," AIAA 20th Thermophysics Conference, Williamsburg, Virginia, June 19-21, 1985, AIAA Paper 85-0994, June 1985.

79. Gupta, R. N., Scott, C. D. and Moss, J. N., "Slip-Boundary Equations for Multicomponent Nonequilibrium Airflow," NASA TP-2452, November 1985.
80. Cleary, J. W., "An Experimental and Theoretical Investigation of the Pressure Distribution and Flow Fields of Blunted Cones at Hypersonic Mach Numbers," NASA TN D-2969, August 1985.
81. Vidal, R. J. and C. E. Wittliff, "Hypersonic Low Density Studies of Blunt and Slender Bodies," Rarefied Gas Dynamics, Vol. II, Supplement 2, Academic Press, New York, 1963, pp. 343-378.
82. Boylan, D., "Laminar Heat Transfer on Sharp and Blunt Ten-Degree Cones in Conical and Parallel Low-Density Flow," AEDC TR-73-106, August 1973.
83. Coleman, G. T., Metcalf, S. C. and Berry, C. J., "Heat Transfer to Hemisphere Cylinders and Bluff Cylinders Between Continuum and Free Molecular Flow Limits," Progress in Astronautics and Aeronautics: Rarefied Gas Dynamics, J. L. Potter, ed., Vol. 51 of 1976, pp. 393-404.
84. Boylan, D., "Laminar Convective Heat-Transfer Rates on a Hemispherical Cylinder in Rarefied Hypersonic Flow," AIAA Journal, Vol. 9, No. 8, August 1971, pp. 1661-1663.
85. John, J. E. A., Gas Dynamics, Allyn and Bacon, Inc., Boston, 1978.

## APPENDIX A

### MASS FLUX CONSERVATION

Of primary importance in the modeling of fluid motion is the conservation of mass. By definition, a mass flux is an amount of mass that flows across a unit area per unit time. Non-reacting physical molecules do not change mass as they travel, however, computational molecules in one part of the computational domain may not have the same physical mass representation in another part of the computational domain. This results from computational regions where the number of physical molecules per computational molecule is different for each region and introduces an additional computational effort as mass is no longer conserved across flux boundaries.

A computational molecule moving through a set of cells in a given region approximates the movement of a constant (but large) number of physical molecules. The number of real molecules represented by a model molecule ( $F_{num}$ ) and the prescribed time step ( $dt_m$ ) are maintained as constant throughout each region. A computational domain where  $F_{num}$  is identical for each region is not feasible from a computation point of view because a constant value throughout the computation domain results in large population gradients when the flowfield density gradients are large. The value of  $F_{num}$  may vary regionally to avoid large computation times not required in low density portions of the flowfield

and that places less demand on computer memory in representing the physical molecules in high density portions of the flowfield. Particles that enter a new region (with a different value of  $F_{\text{num}}$ ) result in the creation (or destruction) of computational molecules to properly simulate mass flux across the boundary. Numerical solutions of the steady flow are computationally efficient by requiring only the mass  $F_{\text{num}}/dt_m$  to be a constant throughout the flow domain and allowing  $F_{\text{num}}$  to vary such that the number of model molecules per cell remains nearly constant. This speeds up the flow time for regions that are relatively free of collision phenomena and it permits regions near surfaces to be populated by only a modest number of computational molecules.

Consider a computational surface defined by the line segment between two regions and each region is at a different time in the evolution of the solution. Mass conservation requires the exiting mass flux to be equivalent to the entering mass flux. A unit of mass is represented by a different number of computational molecules, say in regions 1 and 2. A unit of mass in region 1 can be represented by a single computational molecule and the same amount of mass in region 2 can be represented by 10 computational molecules. For the case where mass leaves region 1 and enters region 2, the difference in the regional time steps (here  $dt_m$  in region 1 is ten times the value of DTM in region 2), would cause mass to cross the flux boundary at an inappropriate time. If region 1 at time  $t_1$  allowed mass to enter region 2 at time  $t_2$ , and if the time in region 1 is later than the time in region 2, mass would leave region 1 but never arrive at region 2. In effect, mass would be propagated to an adjoining region before the adjoining region would be ready to receive it. In the limit where the solution has

evolved to the steady state, the mass flux across all region boundaries is no longer a function of time. This implies that a time independent flux of computational particles will be present for all regional boundaries. The only concern is that all boundary fluxes conserve mass from one region to another, and this is achieved by setting the ratio  $F_{num}/dt_m$  (mass flux across the boundary) to a constant for the entire flow domain. Regardless of the regional time differences the problem has evolved to such an extent (in the steady state) that any additional time will result in no change in the mass flux rate; it is a function only of position. Any transfer of mass per unit of time from region 1 will be received in region 2 as the transfer rates are maintained with the ratio  $F_{num}/dt_m$  as a constant without requiring  $F_{num}$  and  $dt_m$  to be identical in all regions.

## APPENDIX B

### KNUDSEN NUMBER

The concept of Knudsen number was created to allow for the scaling of flowfield parameters in a noncontinuum flow. Early attempts [85] provided Knudsen numbers based on the ratio of the Mach number to the Reynolds number which addressed the global flowfield behavior of a vehicle in flight. A second definition is provided by the ratio of the freestream mean free path to a characteristic length such as a body dimension which physically determines the flow. Interpretation of data in terms of the freestream Knudsen number must be viewed with caution when assessing rarefaction effects. This is readily evident for a slender body where the density downstream of the stagnation region may be 100 times smaller than the stagnation point value, as is the case for some of the present calculations. Such a characterization does not account for variations in surface conditions or shock wave strength.

A more appropriate definition for Knudsen number would include a local gradient based on a primary flow variable such as density. One way to include the density gradient in the definition of the characteristic length is to examine the net change in both time and space of density over some physical scale length. This can be achieved with the time derivative which accounts for the time rate of change in density for a fluid while the field is in motion. Thus, the scale

length,  $\lambda$ , can now be defined as

$$\frac{1}{\lambda} = \frac{1}{U\rho} \left( \frac{\partial \rho}{\partial t} + u \frac{\partial \rho}{\partial x} + v \frac{\partial \rho}{\partial y} + w \frac{\partial \rho}{\partial z} \right)$$

where  $\rho$  is the density,  $U$  is the local velocity and  $u$ ,  $v$  and  $w$  are velocities in the  $x$ ,  $y$  and  $z$  directions. For the current work, only the steady state two-dimensional cases are considered and this results in the first and last terms becoming zero. If a body normal coordinate system is used, a further simplification can be made yielding

$$\frac{1}{\lambda} = \frac{1}{\rho} \frac{d\rho}{dz}$$

Probstein [10,11] has provided an estimate of the size of Knudsen number for various flow regimes. In his papers,  $\epsilon$  is referred to as the scaling factor for Knudsen number and is based on the ratio of the freestream density to the stagnation density. Vorticity interaction regime Knudsen numbers are much smaller than  $\epsilon$ . The viscous layer Knudsen number is smaller than the square root of  $\epsilon$  and Knudsen numbers much smaller than unity are typical of the incipient merged layer regime. Knudsen number is less than unity for the fully merged layer and larger than unity for the transitional layer regime.

Knudsen numbers become large when the mean free path becomes large (as is the case for low densities), or when the characteristic dimension is small (as is the case for a sharp leading edge). In either case, larger Knudsen numbers are indicative of rarefied gas conditions.



## BIOGRAPHY

V. Cuda Jr. was born in Fort Monroe, Virginia, on September 13, 1956. He enrolled in the Department of Mechanical Engineering at Old Dominion University in Norfolk, Virginia, where he received his Bachelor of Science Degree in May 1980. He continued his education at Old Dominion University and received his M. E. degree in December 1982. He enrolled in the Ph.D. Program in Mechanical Engineering at Old Dominion University in January 1983. He is employed as a Research Associate in the Aerothermodynamics Branch at the NASA/Langley Research Center in Hampton, Virginia.